Analysis of uncertainty sources in DNS of a turbulent mixing layer using Nek5000

Juan D. Colmenares F.[1] and Svetlana V. Poroseva[2]
The University of New Mexico, Albuquerque, NM 87131

Yulia T. Peet[3]
Arizona State University, Tempe, AZ 85287

and

Scott M. Murman[4]
NASA Ames Research Center, Moffett Field, CA 94035

Understanding spatial development of a turbulent mixing layer is essential for various aerospace applications. However, multiple factors affect physics of this flow, making it difficult to reproduce results of experiments in simulations. The current study investigates sensitivity of direct numerical simulation (DNS) of such a flow to computational parameters. In particular, effects of a time step in a temporal discretization scheme, dimensions of the computational domain, and the laminar boundary layer characteristics at the splitter plate trailing edge are considered. Flow conditions used in DNS are close to those from the experiments by Bell & Mehta (1990), where untripped boundary layers co-flowing on both sides of a splitter plate mix downstream the plate. No artificial perturbations are used in simulations to trigger the flow transition to turbulence. DNS are conducted using the spectral-element code Nek5000.

Nomenclature

h	=	thickness of the splitter plate at the trailing edge
K	=	turbulent kinetic energy integrated across the mixing layer
L_x, L_y, L_z	=	computational domain dimension in the streamwise, transverse, and spanwise directions
L_x^{ML}	=	length of the mixing layer region in the computational domain
N	=	polynomial order of the Lagrange interpolants
N_s	=	number of snapshots
p	=	pressure
Re_δ	=	Reynolds number with respect to the boundary layer thickness, $U_\infty \delta_{99}/\nu$
Re_θ	=	Reynolds number with respect to the boundary layer momentum thickness, $U_\infty \theta/\nu$
Re_ω	=	Reynolds number with respect to the mixing layer vorticity thickness, $\Delta U \delta_\omega/\nu$
U, V, W	=	streamwise, transverse, and spanwise components of the instantaneous flow velocity
U_∞	=	free-stream velocity
U_1, U_2	=	free-stream velocity of high- and low-speed streams respectively

[1] Graduate Student, Mechanical Engineering, MSC01 1104, 1 UNM Albuquerque, NM 87131-00011, AIAA Student Member.
[2]Associate Professor, Mechanical Engineering, MSC01 1104, 1 UNM Albuquerque, NM 87131-00011, AIAA Associate Fellow.
[3]Assistant Professor, Aerospace Engineering & Mechanical Engineering, Arizona State University, 501 E. Tyler Mall, Tempe, AZ 85287-6106, AIAA Member.
[4] Aerospace Engineer, NASA Ames Research Center, Moffett Field, CA 94035.

U_c = centerline velocity, $(U_1 + U_2)/2$
u, v, w = velocity fluctuations in streamwise, transverse, and spanwise directions
x, y, z = streamwise, transverse, and spanwise coordinates
δ_{99} = boundary layer thickness at the splitter plate trailing edge
δ_1 = boundary layer thickness at the splitter plate trailing edge (high-velocity side)
δ_2 = boundary layer thickness at the splitter plate trailing edge (low-velocity side)
δ_{ML} = mixing layer thickness
δ_ω = mixing layer vorticity thickness, $\Delta U/(\partial\langle U\rangle/\partial y)$
ΔU = velocity difference, $U_1 - U_2$
$\mathbf{u}$ = instantaneous velocity vector
∇ = gradient operator
η_K, τ_K = Kolmogorov length and time scales
θ = momentum thickness, $(1/\Delta U^2)\int_{-\infty}^{\infty}(U_1 - \langle U\rangle)(\langle U\rangle - U_2)\,dy$.
ν = kinematic viscosity
ε = dissipation rate of the turbulent kinetic energy
τ_F = flow-through time, L_x^{ML}/U_c
ω = vorticity
$\langle \dots \rangle$ = averaged value of quantity

I. Introduction

TURBULENT mixing layers formed between two parallel streams of different velocities have long been studied due to their important role in various aerospace applications [1,2]. However, their accurate prediction still remains a challenge, as these flows are very sensitive to variations in the flow parameters. As a result, data obtained in the wind tunnel experiments are specific for a wind tunnel and different from those in applications. Simulations allow for more control of flow parameters, but they can only approximately match those in experiments due to uncertainties in experiments and in simulations [3].

Direct numerical simulation (DNS) is the most accurate approach to simulating turbulent flows in a sense that the model form of uncertainty is eliminated from such simulations. Yet, uncertainties associated with this numerical procedure remain and are difficult to quantify [4]. In our previous work [5], we reviewed standard [6] and more recent [7,8] methods to estimate uncertainty in DNS, and proposed a new method, RANS-DNS simulations, which is more reliable, accurate, and easy to implement framework for such a purpose.

In RANS-DNS simulations, the Reynolds-averaged Navier-Stokes (RANS) equations are solved, with the equation terms being substituted with DNS data for the corresponding terms. When RANS-DNS simulations were conducted in planar wall-bounded turbulent flows such as a channel flow and a zero-pressure gradient boundary layer over a flat plate using DNS data from [9-11], it was found that errors in such data were significant for their use in such simulations. The following work [12] demonstrated that statistical errors are unlikely to be the leading source of uncertainties in DNS data. That is, uncertainties in numerical procedures used in DNS have to be explored further, with the grid resolution near a wall raising questions in particular.

The grid sensitivity analysis in application to DNS is not an easy task due to the DNS cost, but also because the grids used in [9-11] had already been generated using the best practices in the field. Until there is better understanding of this subject, we have decided to proceed with the uncertainty analysis in DNS of a free shear flow, where wall effects on the mixing layer development can be eliminated from consideration. A spatially developing turbulent mixing layer between two co-flowing laminar boundary layers was chosen for the study. Another goal that we pursue by conducting DNS in a mixing layer is to collect high-order velocity moments (through the fifth order) to validate truncated Gram-Charlier series expansions as a model for the probability density function (PDF) of a turbulent flow field in free shear flows. Previously, the truncated Gram-Charlier series expansions have been confirmed as a valid representation of PDF in wall-bounded turbulent flows through experiments and in DNS (see, e.g., [13]) , but to the best of our knowledge, no data required for such an analysis is currently available in free shear flows. Thus, our DNS will compensate for this gap of knowledge. Understanding uncertainty in DNS results will add a value to the dataset. The current paper continues our previous effort [14] in this direction.

Several uncertainty sources were previously investigated in DNS of a turbulent mixing layer. In particular, studies of a spatially developing two-dimensional mixing layer [15] and a temporarily evolving three-dimensional mixing layer [16] showed that the nature and magnitude of flow perturbations imposed at the inflow strongly affect the flow development and turbulence statistics. When co-flowing boundary layers separated by a splitter plate are used as inflow conditions in simulations of a spatially developing mixing layer, the plate thickness at the trailing edge and the

trailing edge shape have a significant effect on the flow features and turbulence intensity [14,17]. Results of DNS were also found to be sensitive to the spanwise size of the computational domain [14]. Overall, due to the simulation cost, there is only a limited number of studies on the uncertainty analysis in DNS of a mixing layer and particularly, of a spatially developing mixing layer. The current study is a contribution to this field.

The flow conditions in our simulations were specified to closely match those in experiments [18], where co-flowing untripped nominally laminar boundary layers formed on both sides of a splitter plate, mix downstream the plate. By allowing the boundary layers to spatially develop over the plate, effects of the trailing edge thickness and shape are taken into account. More control is gained over the boundary layer characteristics and the flow structure at the plate trailing edge. No artificial flow perturbations are used in the simulations to trigger the flow transition to turbulence. This eliminates uncertainties associated with noise generation and seeding perturbations in a flow.

Simulation parameters that vary in the study are the time step in a temporal discretization scheme, boundary layer characteristics at the trailing edge of the splitter plate, and dimensions of the computational domain. The choice of parameters was driven by a search for their optimal combination for conducting cost-effective accurate DNS in a domain long enough to achieve a self-similar regime in a turbulent mixing layer. The initial domain used in [14] was found to be short in the streamwise direction for this purpose.

Two grids were used in the simulations: one from [14] and the other with higher resolution of the wake behind the splitter plate and the mixing layer area. Possible effects of the grid resolution on the simulation results are discussed in the paper, but their detailed analysis was not among the objectives of the current study.

Simulations were conducted using the spectral-element method [19] implemented in the Nek5000 code [20].

II. Numerical method

The non-dimensional incompressible Navier-Stokes equations are solved in their weak form as described in [21] with the code Nek5000 [20], which utilizes spectral element methods (SEM) [19]. The SEM $P_N - P_N$ formulation is used for this study, where solutions for velocity and pressure are both in the space of N^{th}-order Legendre polynomial interpolants, to ensure continuous velocity and pressure fields across the computational domain.

The temporal-discretization scheme in Nek5000 utilized in the simulations is based on a high-order splitting method [22] for decoupling pressure and velocity fields. This method uses a characteristics-based time-stepping scheme for non-linear (convective) terms in combination with an implicit third-order backward difference scheme (BDF3) for viscous terms. In the characteristics-based time-stepping scheme, the solution is calculated along the path lines (or characteristics) associated with the convecting velocity field $\mathbf{u}$. The scheme allows for time steps larger than those required by conventional explicit approaches, where time step is typically constrained by the Courant-Friedrichs-Levy (CFL) condition of $CFL = |\mathbf{u}|\Delta t/\Delta x < c$, where Δt is the size of the time step and Δx is the grid spacing, calculated here based on the Gauss-Legendre-Lobatto quadrature points. A particular value of the constraint c depends on a particular discretization scheme used. In the current characteristics-based approach, this CFL constraint is relaxed.

Determining the values of $\mathbf{u}$ along the characteristics at previous time steps usually involves off-grid interpolations, which are computationally costly. This can be bypassed by using the operator-integration factor scheme (OIFS), which is of the third-order accuracy [23]. In this approach, the values of $\mathbf{u}$ along the characteristics are found by solving an initial-boundary value problem, which uses information readily available at the grid points and thus, avoiding interpolation along characteristics. This approach is used in simulations for the current study. Hereafter, we will refer to the temporal-discretization scheme described above in combination with the OIFS scheme as the OIFS scheme.

Simulations were also attempted with the EXT3/BDF3 scheme available in Nek5000. This scheme employs the explicit third-order extrapolation scheme for non-linear terms and BDF3 for viscous terms. However, the scheme was found unstable in our simulations. A reason for that is currently unknown, as due to limited resources, we could not investigate it in detail.

Aliasing errors are eliminated when computing the non-linear terms in the Navier-Stokes equations using over-integration [21], where non-linear terms are integrated exactly by computing them on a fine grid which contains $3(N + 1)/2$ Gauss-Legendre (GL) quadrature points.

III. Computational setup

Experiments of Bell and Mehta [18] were used in the study to specify dimensions of computational domains and the flow conditions. In the wind tunnel experiments, two boundary layers formed at the sides of a tapered splitter plate merged at the sharp trailing edge of the plate. The boundary layers were tripped or untripped. The latter case resulted in nominally laminar boundary layers at the splitter plate trailing edge. Table 1 provides the boundary layer characteristics for the untripped case, which were used to guide the current simulations. The table data were obtained upstream of the trailing edge at 1.2 cm ($3\delta_{99}$) (no experimental data are available for the trailing edge). In simulations,

these data are used as a reference at the trailing edge. Other discrepancies between experiments and simulations are discussed in Section IV B.

Table 1. Experimental boundary layer parameters at the splitter plate trailing edge [18].

Condition	U_∞, m/s	δ_{99}, cm	θ, cm	Re_δ	Re_θ
High-speed side	15	0.40	0.053	3962	525
Low-speed side	9	0.44	0.061	2611	362

A. Dimensions of Computational Domains

Six different computational domains are used in this study. They all have the same cross-section in the (*x*,*y*)-plane shown in Fig. 1. In the figure, the thick black line represents the splitter plate. Dimensions L_1 and L_2 are the development lengths of the high- and low-speed boundary layers, respectively. The development region, L_3, of length $10\delta_1$ is added upstream of the splitter plate to avoid the singularities in boundary conditions. The mixing region begins at the trailing edge of the plate and has length L_x. The domain geometry does not vary in the spanwise direction.

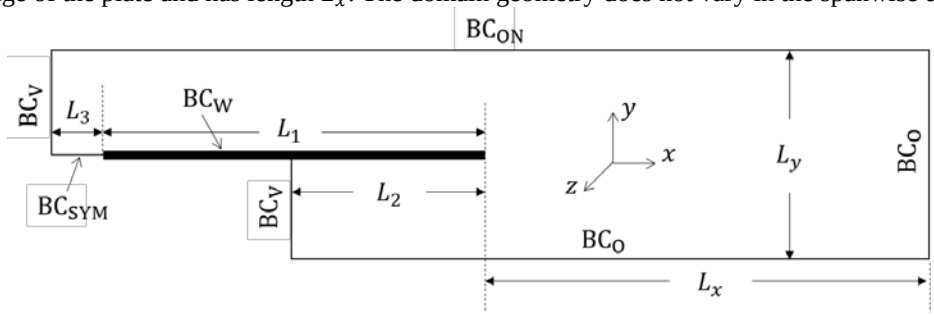

Fig. 1 Computational domain geometry. Boundary conditions: BC_O – outflow, BC_{ON} – outflow/normal, BC_V – uniform velocity, BC_W – wall (no-slip), BC_{SYM} – symmetry (free-slip).

Dimensions of the domains are provided in Table 2. The splitter plate trailing edge corresponds to $x = 0$. The *z*-values vary from 0 to the maximum L_z-value in a domain. Locations corresponding to $y = 0$ are at the splitter plate bottom in Cases I-IV and at the middle of the plate in Cases V and VI.

Table 2. Simulation cases and dimensions of computational domains.

	Description	L_x/δ_1	L_y/δ_1	L_z/δ_1	L_1/δ_1	L_2/δ_1
Case I	Small domain [14]	170	2 × 35	23.4	160	76
Case II	Updated small domain	170	2 × 35	23.4	175	140
Case III	Updated small domain reduced in *y*	170	2 × 25	23.4	175	140
Case IV	Updated small domain extended in *y*	170	2 × 45	23.4	175	140
Case V	Large domain	350	2 × 45	40.0	175	140
Case VI	Large domain reduced in *x*	170	2 × 45	40.0	175	140

The Case I domain was used in [14]. However, simulations showed that the laminar boundary layer on the low-speed side of the splitter plate was underdeveloped at the plate trailing edge ($Re_\theta^L = 281$) to compare with the experimental result of 362 (Table 1). The Reynolds number in the laminar boundary layer on the high-speed side at this location was within 4% ($Re_\theta^H = 540$) of its experimental value of 525. Case II was created to improve the agreement with the experimental flow conditions. Dimensions L_x, L_y, and L_z are the same in both cases.

Initial motivation for the domain dimension $L_x = 170\delta_1$ used in Case I (also Cases II-IV) was two-fold: i) to allow transition to turbulence within the computational domain and ii) to make an estimate of the domain length necessary for obtaining a self-similar regime in a mixing layer. In [14], a turbulent mixing layer was achieved in simulations with the Case I domain, but not the mixing layer self-similarity. Therefore, the domain length in the streamwise direction is increased to $L_x = 350\delta_1$ in the current study (Case V). In the experiments, this dimension of the test section was 366 cm ($L_x = 915\delta_1$), with the mixing layer self-similarity being observed around $L_x = 312.5\delta_1$. Following the current paper objectives, results from all cases are presented in the range of $[0, 170\delta_1]$ in the streamwise direction.

The domain transverse dimension of the domai is $L_y = 70\delta_1$ in Cases I and II. With respect to the maximum value of the mixing layer vorticity thickness $\delta_{\omega,max}/\delta_1$, which is equal to 6.22 in these simulations, $L_y/\delta_{\omega,max} = 11.25$. This domain length was assumed to be sufficient based on previous DNS results [25,26], which showed the lack of sensitivity to this parameter in the interval of $6.96 < L_y/\delta_{\omega,max} < 8.3$. In Case III, this dimension was reduced to $L_y = 50\delta_1$ ($L_y/\delta_{\omega,max} = 8.03$) and increased to $L_y = 90\delta_1$ in Cases IV-VI. In Case V with the domain longest in the streamwise direction, $\delta_{\omega,max}/\delta_1$= 6.29 and $L_y/\delta_{\omega,max} = 14.3$. The largest considered L_y of $90\delta_1$ corresponds to the test section dimension of 36 cm in the transverse direction.

In the experiments, the test section dimension in the spanwise direction was 91 cm ($L_z = 227.5\delta_1$). The computational domains used in the Cases I-IV simulations were almost the order of magnitude smaller in this direction: $L_z = 23.4\delta_1$ The corresponding aspect ratio value, $A = L_z/\theta_{max}$, is 14.7 for these cases. Here, θ_{max} is the maximum mixing layer momentum thickness. Based on the criterion $A > 10$ suggested in [27], this value is large enough to have negligible effect on the mixing layer growth rate. Using the same criterion as a reference, the domain dimension is increased $L_z = 40\delta_1$ for Cases V and VI, so that the corresponding *A*-values are 11.4 and 24.7, respectively. That is the criterion for *A* is satisfied in all six domains used in the study. Notice though that the domain spanwise dimension was shown to have a strong effect on simulation results including the mixing layer growth even if the criterion for *A* is satisfied [14]. That is, uncertainty associated with this parameter remains and has to be studied further.

B. Boundary Conditions

In Nek5000, the boundary conditions are applied to the velocity field, while the pressure values at the boundaries are computed [20, 22]. The same boundary conditions as shown in Fig. 1 were used in all simulations presented in the paper. The fixed uniform velocity profile was used at the inlet:

$$U(x = x_{inl}, y, z, t) = \begin{cases} U_1 & if\ y > 0 \\ U_2 & if\ y < 0 \end{cases}; V(x = x_{inl}, y, z, t) = W(x = x_{inl}, y, z, t) = 0, \quad (1)$$

where x_{inl} is the location of the inlet boundary. Normalized velocity values used in all simulations were $U_1/U_\infty = 1$ and $U_1/U_\infty = 0.6$. The no-slip boundary condition was applied everywhere on the splitter plate. The symmetry condition was applied at the lower boundary of the region upstream of the splitter plate. The convective outflow condition, $[p\mathbf{I} + \nabla\mathbf{u}] \cdot \hat{\boldsymbol{n}} = 0$, was applied at the outlet. Here, $\mathbf{I}$ is the identity matrix, and $\hat{\boldsymbol{n}}$ is the unit vector normal to the boundary and directed outwards. The convective outflow condition was also applied at the lower boundary. The outflow-normal condition was applied at the upper boundary. This condition implies that the velocity component normal to the boundary is free ($\partial V/\partial n = 0$), but the tangent velocity components are fixed: $U = U_1,\ W = 0$. The outflow conditions ensure the zero pressure gradient in the streamwise direction. In the spanwise direction, the periodic boundary conditions were used.

C. Initial Conditions

Uniform velocity profiles of free-stream velocities were applied throughout the domain as initial conditions in Cases I, II, V and VI. A single flow realization from Case II at simulation time $t = 500$ was used as initial conditions in Cases III and IV. In the simulations, time is normalized with respect to U_1 and δ_1, i.e. $t = U_1 t^*/\delta_1$, where t^* is the dimensional time and t is non-dimensional. For Case III, a spectrally accurate interpolation of the flow field from Case II was achieved using existing subroutines in Nek5000. For Case IV, the velocity field was interpolated from Case II where data was available ($|y/\delta_1| < 35$), while uniform velocity profiles of free-stream velocities were imposed at the nodes that laid outside of the Case II domain ($|y/\delta_1| > 35$).

D. Grids

Grids used in Cases I-IV are based on the grid from Case I, described in terms of conforming meshing zones depicted and labeled in Fig. 2. Coordinates of the points marked in red in the figure are shown in Table 3. The grid parameters are given in Table 4. In the table, n_x and n_y are the number of elements in the x and y directions, r_x and r_y are the growth rates in each direction, and Δx and Δy are the element sizes in the respective directions. Here, growth rate $r_y = \Delta y^{i+1}/\Delta y^i$ is the ratio between the sizes of adjacent elements Δy^{i+1} and Δy^i, where Δy^i and Δy^{i+1} are in a sequential order in the direction of $+y$. The rate r_x follows the similar definition in the direction of $+x$. Note that description of zones M and N have been omitted, since they are the mirror reflections of zones H and G with respect to $y = 0$.

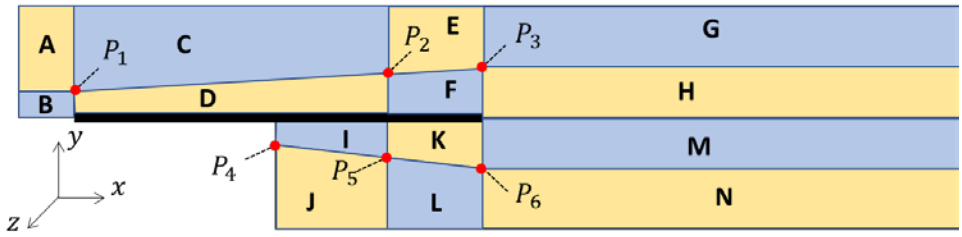

Fig. 2 Meshing zones for Case I.

Table 3 Coordinates of red points in Fig. 2.

Coordinate	P_1	P_2	P_3	P_4	P_5	P_6
x/δ_1	-160	-30	0	-76	-30	0
y/δ_1	4	10.5	12	-4	-8.8	-12

Table 4 Parameters for the Case I grid.

Parameter	A	B	C	D	E	F	G	H	I	J	K	L
n_x	5	5	24	24	11	11	110	110	16	16	9	9
n_y	6	8	6	8	6	8	6	8	8	6	8	6
r_x	0.870	0.870	1.041	1.041	0.890	0.890	1.004	1.004	1.050	1.050	0.920	0.920
r_y	1.150	1.060	1.150	1.060	1.150	1.060	1.150	1.060	0.943	0.870	0.943	0.870
Min. $\Delta x/\delta_1$	1.50	1.50	3.33	3.33	1.74	1.74	1.17	1.17	2.10	2.10	2.34	2.34
Max. $\Delta x/\delta_1$	2.60	2.60	8.40	8.40	5.60	5.60	1.75	1.75	4.58	4.58	4.55	4.55
Min. $\Delta y/\delta_1$	3.54	0.41	2.79	1.03	2.63	1.17	2.63	1.17	0.92	3.00	1.17	2.63
Max. $\Delta y/\delta_1$	7.12	0.58	5.63	1.55	5.30	1.75	5.30	1.75	1.47	6.94	1.75	5.30

A row of rectilinear elements (not listed in the table) was added downstream of the thick plate in the region between zones H and M. In the y-direction, this is an additional element, which size is equal to the splitter plate thickness in order to maintain a conforming grid required by the solver. In the *x*-direction, the number and dimensions of these elements are the same as in the adjacent zones H and M.

The grid for Case II has the same resolution as the Case I grid in the mixing layer region. As L_1 and L_2 are increased in this grid to compare with Case I, two elements are added in zones C and D and eight elements in zones I and J in the x-direction to maintain similar resolution along the plate as in the Case I grid in these zones. In the y-direction, dimensions of the added elements comply with the ratios provided in Table 4 for the corresponding zones.

The grid for Case III is based on that of Case II, with two elements (adjacent to the domain boundaries) being removed in the y-direction from each of the outer regions (A, C, E, G, J, L, N).

To obtain a grid for Case IV, two elements were added in the y-direction to each of the outer regions (A, C, E, G, J, L, N) of the Case II grid. Then, the grid was re-meshed within the new boundaries of the zones using the same vertical growth rates (r_y) shown in Table 4 for the corresponding zones. As a result, the $\min \Delta y$ value was decreased by 8.5% and max Δy was increased by 21% in each altered zone with respect to their values in Table 4. Dimensions of the elements in the *x*-direction were unchanged with respect to the Case II grid. The zones in the inner region (B, D, F, H, I, K, M) were also unchanged with respect to the Case II grid.

Cases I-IV have twenty uniformly distributed elements in the spanwise direction of the size $\Delta z/\delta_1 = 1.17$. The total numbers of grid elements in Cases I-IV are: 82,000, 84,800, 73,000 and 96,600, respectively.

Meshing zones for the Case V grid are shown in Fig. 3, with geometrical and grid parameters listed in Tables 5 and 6, respectively. Description of zones M and N have been omitted, since they are the mirror reflections of zones H and G with respect to $y = 0$. One row of elements was added downstream of the plate, in the region between zones H and M, shown in Fig. 4 in navy blue color. The elements at $x = 0$ have the same thickness as the plate, $h = 0.25$ mm $= 0.0625\ \delta_1$. The element size Δy increases linearly with x until the elements achieve the same thickness ($\Delta y/\delta_1 = 1.53$) as the elements in the neighboring zones H and M at the end of the computational domain ($x/\delta_1 = 350$). In the x-direction, elements have the same sizes and growth rates as those in adjacent zones (H and M), listed in Table 6. As

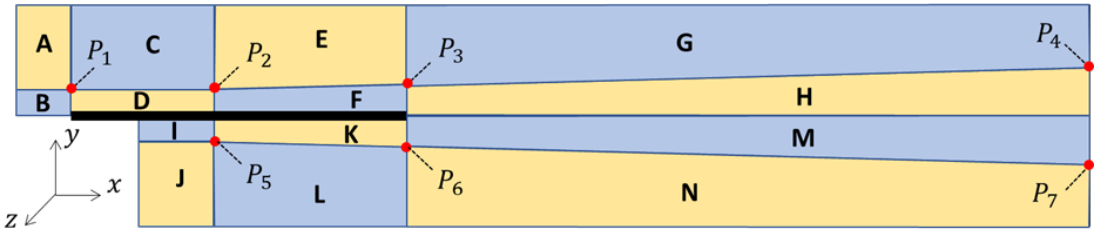

Fig. 3 Meshing zones for Case V.

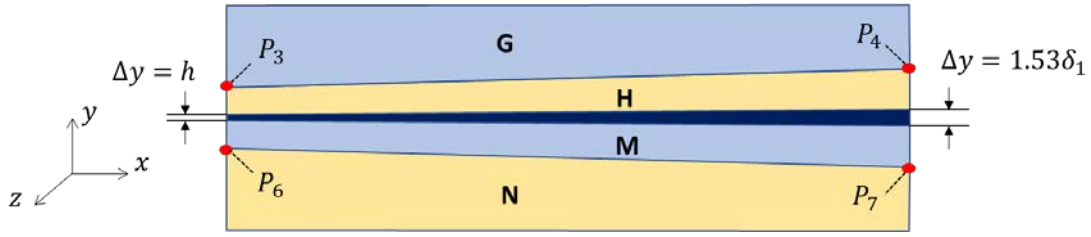

Fig. 4 Schematic view of the single row of elements (shown in navy blue) added in the region between zones H and M in the grids for Cases V and VI.

a result, the splitter plate wake area and the mixing layer region are more refined in the Case V grid than in the Case I grid in the (*x*,*y*)-plane. The grid resolution near the splitter plate trailing edge for both grids is shown in Fig. 5. The grid has thirty four uniformly distributed elements in the spanwise direction, with their dimension in this direction being $\Delta z/\delta_1 = 1.178$.

The grid for Case VI was obtained from the Case V grid by cutting it off at $x/\delta_1 = 170$. The total numbers of grid elements in Cases V and VI are 381,174 and 233,070, respectively.

The grids for Cases I and V that include only spectral elements without collocation points are shown in Fig. 6. Polynomial interpolants of order $N = 11$ were used in all cases to represent the continuous velocity and pressure fields in the computational domain. The number of quadrature points located inside each element is $(N+1)^3$, with the $N+1$ quadrature points being located in each direction based on the distribution of Gauss-Legendre-Lobatto quadrature points in local (elemental) coordinates.

Table 5 Coordinates of the red points in Fig. 3.

Coordinate	P_1	P_2	P_3	P_4	P_5	P_6	P_7
x/δ_1	-175	-140	0	350	-140	0	350
y/δ_1	4	4	7.69	21	-4	-7.69	-21

Table 6 Grid parameters for Case V.

Parameter	A	B	C	D	E	F	G	H	I	J	K	L
n_x	5	5	17	17	27	27	299	299	10	10	25	25
n_y	7	9	7	9	7	9	7	9	9	7	9	7
r_x	0.870	0.870	1.050	1.050	0.926	0.930	1.005	1.005	1.050	1.050	0.931	0.931
r_y	1.100	1.060	1.100	1.060	1.100	1.060	1.100	1.060	0.943	0.909	0.943	0.909
Min. $\Delta x/\delta_1$	1.50	1.50	2.78	2.78	0.91	0.91	0.45	0.45	3.10	3.10	0.91	0.91
Max. $\Delta x/\delta_1$	2.60	2.60	6.06	6.06	6.66	6.66	1.53	1.53	4.80	4.80	5.04	5.04
Min. $\Delta y/\delta_1$	4.32	0.35	4.32	0.35	3.93	0.67	2.53	1.53	0.35	4.32	0.67	3.93
Max. $\Delta y/\delta_1$	7.66	0.55	7.66	0.55	6.97	1.07	4.50	2.44	0.55	7.66	1.07	6.97

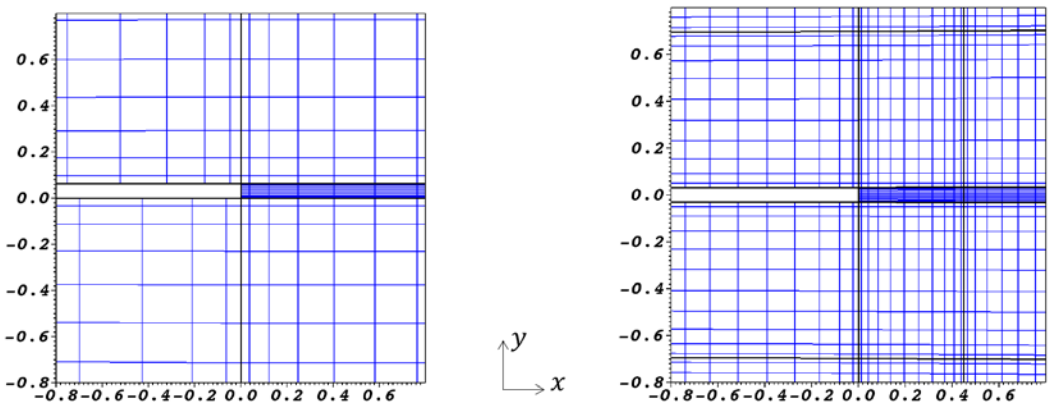

Fig. 5 Spectral element grid (black lines) and quadrature points (intersection of blue lines) near the trailing edge of the plate, a) Case I, b) Case V.

All grids were designed to satisfy the requirement of $(\delta x \cdot \delta y \cdot \delta z)^{1/3} < 4\eta_K \div 8\eta_K$ [28,29], where $\delta x, \delta y, \delta z$ is the average spacing between quadrature points in streamwise, transverse, and spanwise directions, η_K is the Kolmogorov length scale $\eta_K = (\nu^3/\varepsilon)^{1/4}$. Specifically, resolution in Cases I – IV is $(\delta x \cdot \delta y \cdot \delta z)^{1/3} < 5.33\,\eta_K$, while in Cases V-VI, it is $(\delta x \cdot \delta y \cdot \delta z)^{1/3} < 4.9\,\eta_K$ everywhere in the flow.

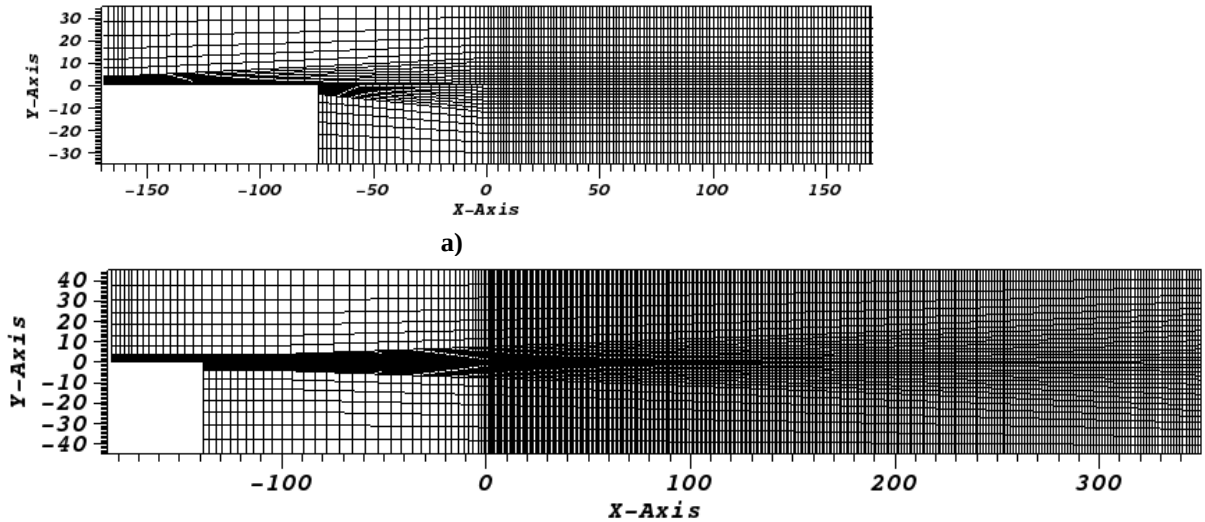

Fig. 6 Grids of spectral elements shown without internal collocation points: a) Case I and b) Case V.

E. Temporal Resolution

Simulations were conducted using the OIFS temporal discretization scheme described earlier. Two different time steps were used in the Case I simulation: $\Delta t = 0.012$ and $\Delta t = 0.02$, which correspond to *CFL* = 0.45 and 0.75, respectively. In Cases II-VI, only the time step of $\Delta t = 0.02$ was used, which yielded *CFL* = 0.75 in Cases II-IV and *CFL* = 1.8 in Cases V and VI.

IV. Results

A. Collection of Statistical Data

Statistics were collected after a flow became statistically stationary. The flow was deemed statistically stationary, when the volume-averaged statistics relevant to the flow kinetic energy: $\langle U^2 \rangle_V$, $\langle V^2 \rangle_V$ and $\langle W^2 \rangle_V$, were stabilized. Here, $\langle \dots \rangle_V$ is the volume average, and U, V, W are components of the instantaneous flow velocity.

In the cases, where simulations started at $t = 0$ (Cases I, II, V and VI), the initial transient period (not used to collect statistics) was $t_{trans} \sim 500$ (normalized by δ_1/U_1 from the experiments [18]). This corresponds to 2.4 flow-through times $\tau_f = L_x/U_c$ in Cases I, II, and VI, and to 1.15 τ_f in Case V. Figure 7 shows the convergence of $\langle U^2 \rangle_V$, $\langle V^2 \rangle_V$ and $\langle W^2 \rangle_V$ in Cases II and V as examples. Vertical dashed lines in the figures indicate the end of the transient period in each case.

Cases III and IV started from the Case II solution at $t = 500$. The convergence of $\langle U^2 \rangle_V$, $\langle V^2 \rangle_V$ and $\langle W^2 \rangle_V$ in these cases is shown in Fig. 8 in comparison with the Case II solution evolution. Transient periods were not taken into account when collecting statistics for these cases. That is, statistics for all cases presented in the current paper were collected during time interval of $t = [500, 2000]$, which corresponds to $7.05\tau_f$ in Cases I-IV and VI, and $3.5\tau_f$ in Case V.

In Case I, instantaneous flow field realizations used to extract statistics were saved every 300 time steps in simulations with $\Delta t = 0.012$ and every 200 time step in simulations with $\Delta t = 0.02$. In Cases I-IV and VI, they were saved every 200 time steps. Due to increased file sizes, raw flow fields in Case V were saved every 500 time steps. No information on correlation coefficients between the flow realizations at different time steps is available at this point.

The computed raw flow fields were post-processed to extract ensemble-averaged statistics:

$$\langle Q(x,y,z) \rangle_{en} = \frac{1}{N_s} \sum_{i=1}^{N_s} Q_i\,(x,y,z), \tag{2}$$

where Q is a quantity to be averaged and N_s is the number of flow realizations or "snapshots". In Case I, where the time step of $\Delta t = 0.012$ was used, the total number of snapshots was $N_s = 419$. In Cases I-IV and VI, which used $\Delta t = 0.02$, a smaller number of flow realization, $N_s = 376$, was available. The number of flow realizations used in Case V was $N_s = 152$.

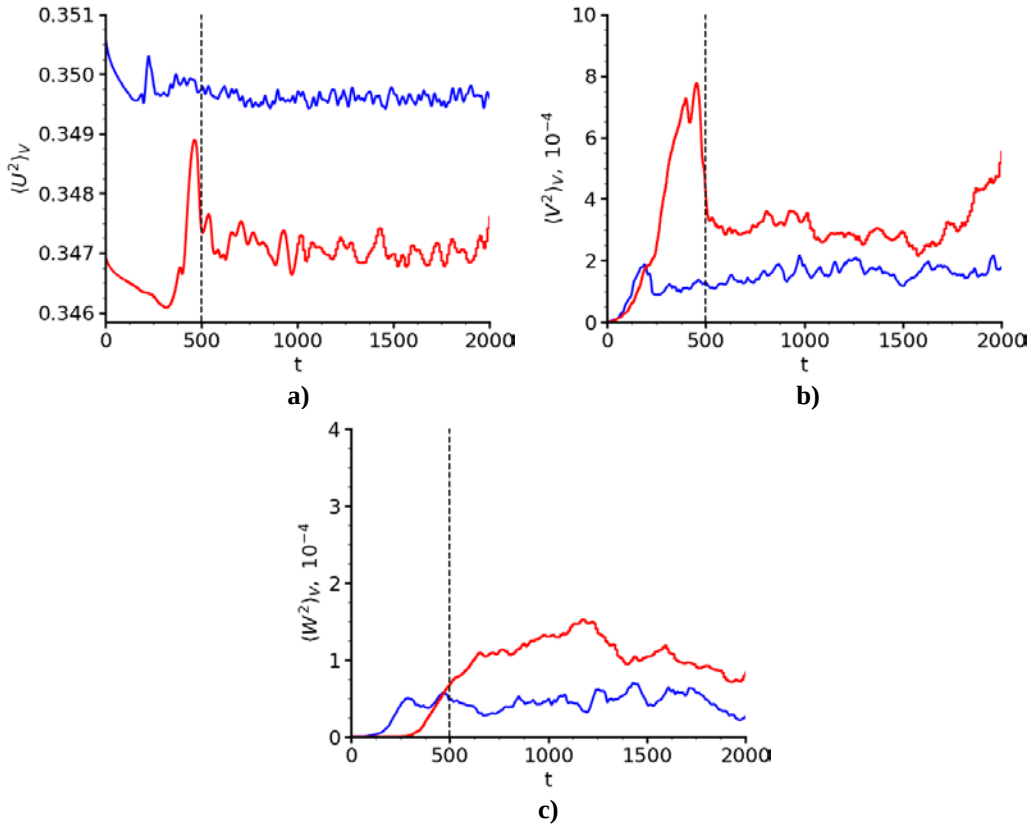

Fig. 7 Time evolution of the volume-averaged statistics relevant to the flow kinetic energy, a) streamwise component, $\langle U^2 \rangle$, b) transverse component, $\langle V^2 \rangle$, c) spanwise component, $\langle W^2 \rangle$. Vertical lines mark $t_{trans} = 500$. Colors: blue – Case II, red – Case V.

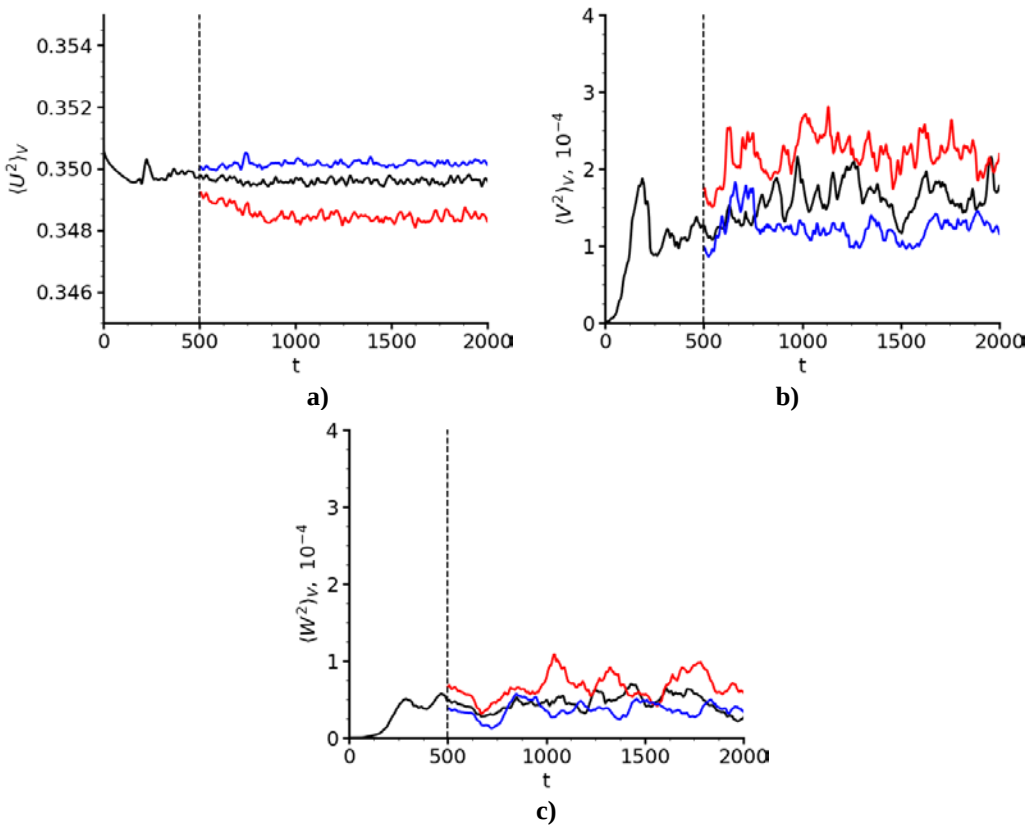

Fig. 8 Time evolution of the volume-averaged statistics relevant to the flow kinetic energy, a) streamwise component, $\langle U^2 \rangle$, b) transverse component, $\langle V^2 \rangle$, c) spanwise component, $\langle W^2 \rangle$. Vertical lines mark $t_{trans} = 500$. Colors: black – Case II, red – Case III, blue – Case IV.

After this step, the ensemble-averaged data were averaged again in the spanwise direction:

$$\langle Q(x,y) \rangle = \frac{1}{L_z} \int_0^{L_z} \langle Q(x,y,z) \rangle_{en} \, dz. \tag{3}$$

This step utilizes the simulated flow homogeneity in the spanwise direction to improve the quality of collected statistics. Integration is done using the Gaussian quadrature over the Gauss-Lobatto-Legendre quadrature points.

B. On Comparison of Experimental and DNS data

In the following sub-sections, statistics collected from DNS are compared with experimental data, where available. However, due to unavoidable differences in experimental settings and simulations, differences in the flow development and as a consequence, in the results have to be expected. In the experiments, for example, the "nominally laminar" boundary layers had a well-defined three dimensional structure, with turbulence being present before the boundary layers left the splitter plate trailing edge [18,24]. Free-stream turbulence reported in [18] is between 0.05% and 0.15%. This is seen when comparing the shape factors and the skin friction coefficients of experimental boundary layers at the trailing edge of the splitter plate with their values in the corresponding Blasius laminar boundary layers (Table 7). The boundary layer at the low-speed side of the plate deviates the most from the Blasius solution. A difference in the skin friction coefficient values from the same experimental setup, but reported in different publications is also noticeable, but its origin is unclear.

Figure 9a shows streamwise variations of the maximum value of the shear stress, $\langle uw \rangle$, averaged in the (y, z)-plane. The maximum peak value of $\langle uw \rangle$ is near the splitter plate trailing edge, indicating that experimental boundary layers are three dimensional. In a planar laminar flow, this shear stress is equal to zero. [18]. The structure of experimental boundary layers and their contamination with turbulence may be responsible for the virtual origin of the mixing layer being upstream from the trailing edge [18].

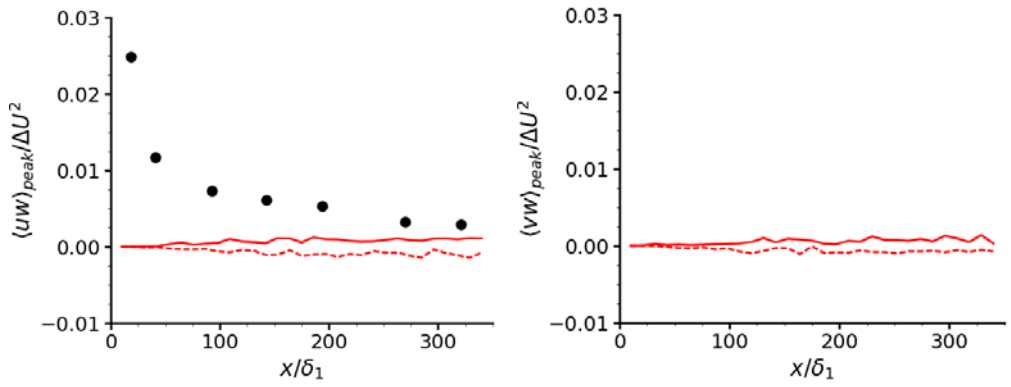

Fig. 9 Variations of maximum and minimum values of the shear stresses a) $\langle uw \rangle$ and b) $\langle vw \rangle$ in the (y, z) plane in the x-direction. Notation: circles – maximum values from the experiments [18], lines –DNS data from Case V. Solid lines – maximum values, dashed lines – minimum values.

Deviation of the experimental boundary layers from planar laminar conditions can be linked to constructional features of wind tunnels such as screens [24]. However, constructional features and upstream turbulence effects cannot be accurately reproduced in numerical simulations and are not attempted in the current study to avoid adding uncertainty in simulations.

Table 7. Experimental boundary layer characteristics close to the splitter plate trailing edge.

		Shape factor, H		**Skin friction coefficient, $C_f \times 10^3$**		
Condition	**U_∞, m/s**	**Refs. [18,24]**	**Blasius solution**	**Ref. [18]**	**Ref. [24]**	**Blasius solution**
High-speed side	15	2.52	2.59	0.72	0.87	0.84
Low-speed side	9	2.24	2.59	0.91	1.56	1.22

The splitter plate shape and dimensions used in the simulations also differ from those in the experiments. The sharp-ended plate used in the experiments was tapered, with its thickness varied from 5 cm at the base to 0.5 mm at the trailing edge [24] (0.25 mm in [18]). In simulations, the splitter plate is sharp-ended, but has uniform thickness of 0.25 mm.

The other source of uncertainty is a difference in dimensions of the wind tunnel test section ($915\delta_1 \times 90\delta_1 \times 227.5\delta_1$ in the x, y, and z directions, respectively) and those of the computational domains (Table 2). This affects the flow conditions at the boundaries of a computational domain and as a result, the mixing layer development. In addition, the wall on the low-speed side of the experimental test section was flexible to control the streamwise pressure gradient in the experiments. Other boundary conditions were used in the simulations to ensure that the mean pressure gradient is equal to zero in the streamwise direction as described in Section III B.

In simulations, the boundary layers at the trailing edge of the splitter plate are planar and laminar. As an example, velocity profiles at the plate trailing edge are compared with the Blasius solutions in Fig. 10 for Case II. Case I in this respect was discussed in [14]. Corresponding velocity profiles in Cases III-VI overlap with those in Case II.

All Reynolds stresses are zero at this location in all simulations. The shear stresses $< uw >$ and $< vw >$ from Case V are shown in Fig. 9. Similar results for these stresses were obtained in other cases as well. Like $< uw >$, the shear stress $<$

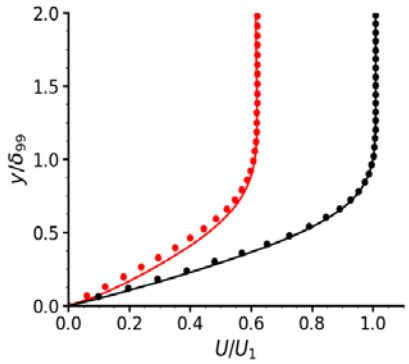

Fig. 10 Profiles of the boundary layers at the trailing edge of the splitter plate in Case II simulations. Notations: lines - DNS, circles – Blasius solution. Colors: black – high-speed side, red – low-speed side.

$vw >$ is an indicator whether a flow is planar and thus, important for collecting. Unfortunately, both shear stresses are rarely provided in datasets for a mixing layer, which contributes in difficulties associated with the development and validation of turbulence models in this flow. Other Reynolds stresses do not appear until $x > 10\delta_1$ in all cases as shown in the following sub-sections.

Table 8 lists non-dimensional characteristics of the boundary layers at the splitter plate trailing edge for all cases. Hereafter, all length scales are normalized with respect to $\delta_1 = 0.4\ cm$, the experimental boundary layer thickness at the trailing edge of the splitter plate with the high-speed flow over it. Velocities are normalized with respect to the experimental high-speed free-stream velocity $U_1 = 15\ m/s$. Notice that for the time step $\Delta t = 0.012$ in Case I, Table 8 contains corrections of typos for θ made in [14] for this case.

In Cases II-VI, some variation in the values of the boundary layer thickness and its momentum thickness is observed, but when rounded off to two decimal digits, they correspond to those in the table. When comparing with the experimental values in Table 7, the boundary layer thickness and its momentum thickness are within 1.5 and 2.5%, respectively, on both sides of the splitter plate for these cases. In Case I, they are within 5% at the high-speed side and within 25% at the low-speed side of the plate.

Table 8. Laminar boundary layer parameters at the splitter plate trailing edge.

Case	Condition	U_∞/U_1	δ_{99}/δ_1	θ/δ_1	Re_δ	Re_θ	Shape factor, H	Skin friction coefficient, $C_f \times 10^3$
I	High-speed side	1.0	0.95	0.136	3746	540	2.34	1.25
I	Low-speed side	0.6	0.74	0.118	1751	281	2.16	3.14
II-VI	High-speed side	1.0	0.99	0.133	3930	565	2.35	1.15
II-VI	Low-speed side	0.6	1.01	0.153	2412	364	2.22	2.48

The shape factor, H, and the skin friction coefficient, C_f, obtained in all simulations show evidence of a slightly favorable pressure gradient at the trailing edge of the plate, when compared against the Blasius solution. In preliminary simulations of a boundary layer over a flat plate without the mixing layer being present, the Blasius solution was reproduced exactly using the same grids and the flow conditions as used in the current simulations. This suggests that deviation of the boundary layers conditions in the simulations from the Blasius solution is due to the mixing layer development downstream from the splitter plate trailing edge affecting the upstream flow. Differences in the values of H and C_f obtained in the simulations and in the experiments can be explained by differences in the structure of the boundary layers and their turbulence level as discussed above.

C. Statistics Convergence

The purpose of this study is to analyze sensitivity of the simulation results to variations in simulation parameters. A solution response to a parameter change can be recognized prior the solution statistically converged. In this regard, statistics that did not substantially change with increasing the simulation time were deemed sufficient for the qualitative sensitivity analysis. Temporal convergence of statistics obtained in the Case I simulations with $\Delta t = 0.012$ was discussed in [14] and was found acceptable for the current study. Here, the convergence of statistics obtained with the larger time step, $\Delta t = 0.02$, in Cases I and V is discussed. Case I is shown to demonstrate that the results for this case are still acceptable even though the simulations were conducted with the larger time step. Case V has the largest domain and the least number of samples used for the data averaging. Other cases will be shown in the presentation.

For the convergence analysis, data were collected over two time intervals – $T_1 = [500, 1700]$ and $T_2 = [500, 2000]$ – and compared with each other, separately for Cases I and V. In Case I, this corresponds to 300 and 376 flow realizations used in the averaging procedure, respectively. In Case V, the corresponding numbers are 120 and 152.

Statistics, which convergence is investigated, are the mixing layer thickness, streamwise evolution of the normal Reynolds stresses integrated across the mixing layer, and the Reynolds stresses, normal and $< uv >$, at $x/\delta_1 = 160$, far away from the splitter plate. This location is close to the domain outlet ($x/\delta_1 = 170$) in Cases I-IV and VI.

Hereafter, the mixing layer thickness, δ_{ML}, is defined as in [18]:

$$\delta_{ML} = (y - y_0)/\eta, \tag{4}$$

where this parameter is obtained by computing the least-squares fit of the mean velocity profile to the error function profile shape:

$$(\langle U\rangle - U_2)/\Delta U \approx [1 + \mathrm{erf}(\eta)]/2. \tag{5}$$

In (4), y_0 is the centerline of the mixing layer also calculated by the least-square fitting procedure.

Reynolds stresses integrated across the mixing layers are determined as follows:

$$K_x(x) = \frac{1}{\Delta U^2}\int_{-Ly/2}^{Ly/2}\langle u^2\rangle\ dy, \tag{6}$$

$$K_y(x) = \frac{1}{\Delta U^2}\int_{-Ly/2}^{Ly/2}\langle v^2\rangle\ dy, \tag{7}$$

$$K_z(x) = \frac{1}{\Delta U^2}\int_{-Ly/2}^{Ly/2}\langle w^2\rangle\ dy. \tag{8}$$

Note that the values in the brackets in the Eqs. (6)-(8) are already spanwise-averaged according to Eq. (3). The streamwise growth of the mixing layer thickness is not affected by increasing the time interval used for the data averaging in both cases (Fig. 11). The normal Reynolds stresses integrated across the mixing layer particularly, K_y, show more sensitivity to the time interval length and more so in Case V (Figs. 12,13) as expected. In figures 12 and 13, experimental values of $K_x, K_y,$ and K_z (shown by circles) were approximated by numerical integration of the experimental data for the Reynolds stresses using the trapezoidal rule.

The Reynolds stresses obtained in Case I at the streamwise location $\boldsymbol{x/\delta_1 = 160}$ (Fig. 14) are practically identical, when averaged over different time intervals. Similar conclusion is applied to all Reynolds stresses, but $< \boldsymbol{w^2} >$ in Case V (Fig. 15). The maximum value of $< \boldsymbol{w^2} >$ in this case is reduced by ~10% when the time interval for the data averaging increases.

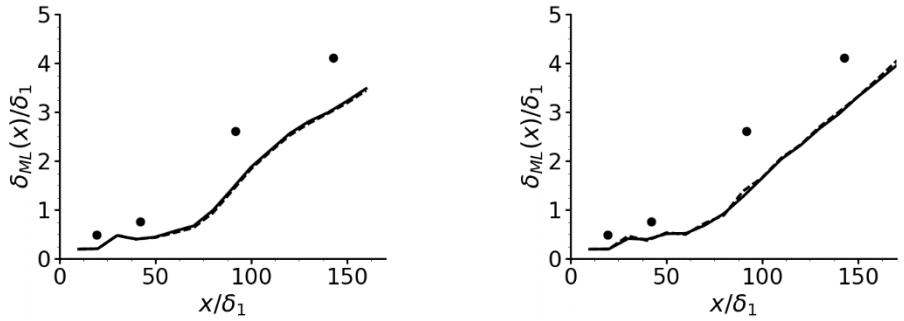

Fig. 11 Mixing layer thickness: a) Case I, b) Case V. Notations: solid lines – DNS data collected over the time interval T_2, dashed lines –DNS data averaged over T_1, circles – experimental data [18].

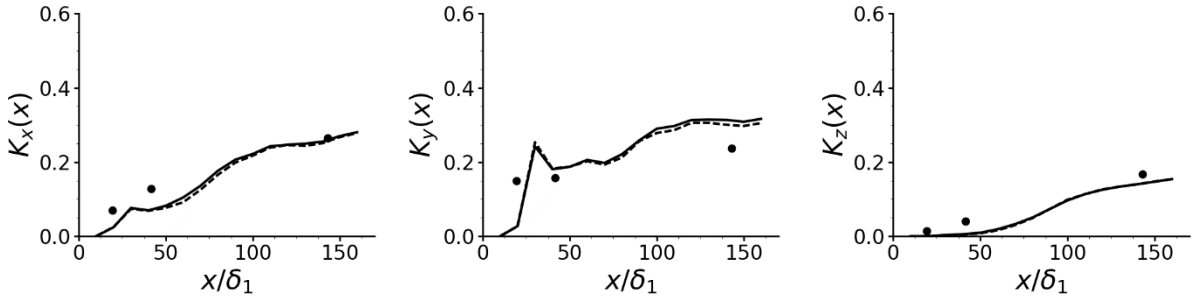

Fig. 12 Streamwise evolution of the Reynolds stresses integrated across the mixing layer in Case I. Notations are the same as in Fig. 11.

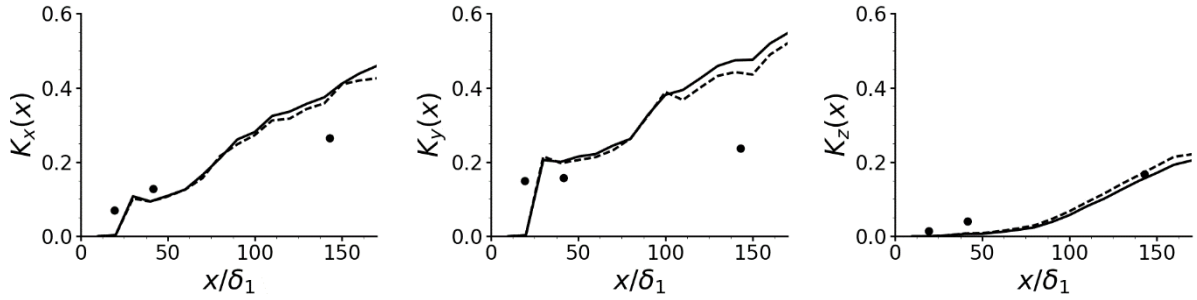

Fig. 13 Streamwise evolution of the Reynolds stresses integrated across the mixing layer in Case V. Notations are the same as in Fig. 11.

Overall, the qualitative analysis of statistics obtained by averaging over two different time intervals demonstrates that the data obtained over the larger interval, $T_2 = [500, 2000]$, are acceptable for comparison of the simulation results from different cases. Results for K_y and $< w^2 >$ from Case V will be clarified in the following work.

D. Time Step

In this sub-section, influence of the time step in the temporal discretization scheme on the DNS results is discussed. For this analysis, simulations were conducted with two different time steps $\Delta t_1 = 0.012$ and $\Delta t_2 = 0.02$ using the computational domain and the grid for Case I. With these time steps, the *CFL* values are 0.45 and 0.75, respectively. That is, the traditional stability criterion for the corresponding explicit scheme of the same order of accuracy in Nek5000, BDF3/EXT3, $CFL = 0.5$, is satisfied with Δt_1, but not with Δt_2. The OIFS scheme in Nek5000 permits such simulations and as a result, the simulation cost can be substantially reduced. On the other hand, some of smaller scales may be filtered in the process, which, depending on the filtered scales origin, physical or numerical, may or may not be beneficial for the quality of simulation results.

The flow characteristics considered in this and following sub-sections are the mixing layer growth characterized by its thickness and momentum thickness, streamwise mean flow velocity, and streamwise evolution of the normal Reynolds stresses and their sum integrated across the mixing layer, as well as the Reynolds stresses at several locations

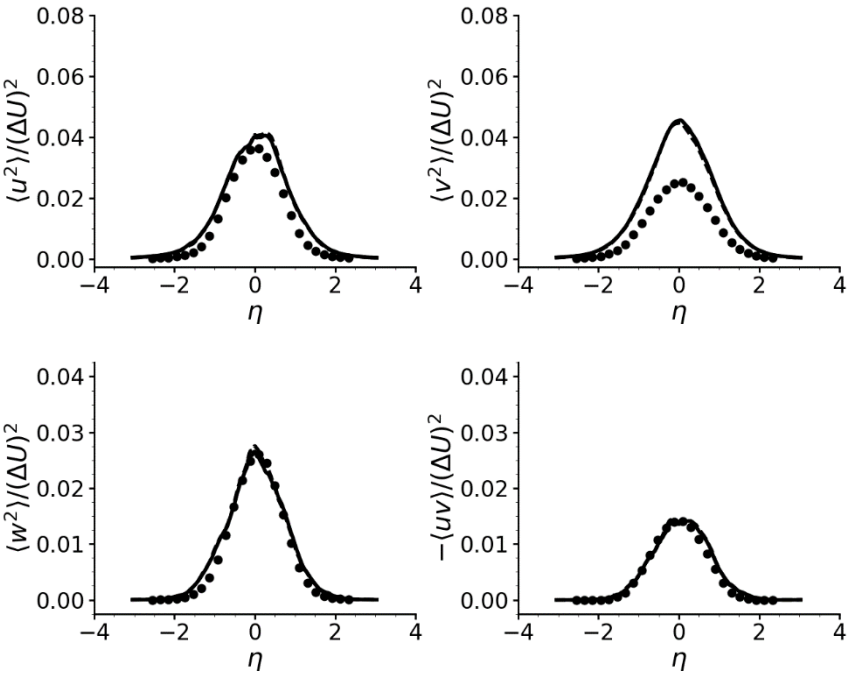

Fig. 14 Reynolds stresses from Case I at $x/\delta_1 = 160$. Notations are the same as in Fig. 11.

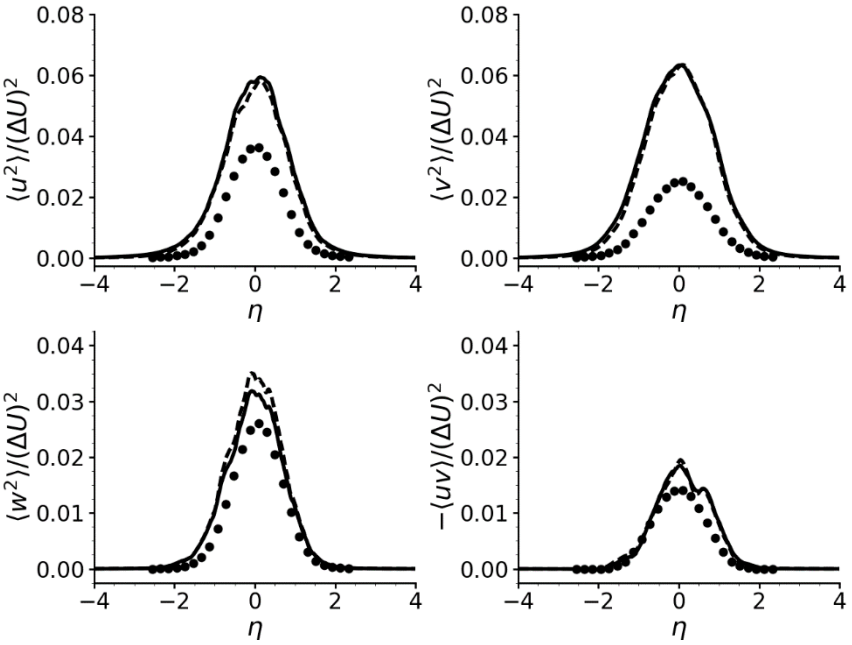

Fig. 15 Reynolds stresses from Case V at $x/\delta_1 = 160$. Notations are the same as in Fig. 11.

in the streamwise direction. Snapshots of instantaneous vortex structures visualized using λ_2-criterion [30] are also presented. The mixing layer momentum thickness is defined as in [26]:

$$\theta_{ML} = (1/\Delta U^2)\int_{-\infty}^{\infty}(U_1 - \langle U\rangle)(\langle U\rangle - U_2)\,dy. \tag{9}$$

Figure 16 compares the mixing layer thickness and its momentum thickness obtained at the two time steps. In the figure, black and red lines correspond to Δt_1 and Δt_2, respectively. Experimental data are shown by circles. The figure demonstrates that the time step affects both parameters far downstream from the splitter plate, with the mixing layer growth obtained with the smaller time step being closer to the experimental data.

Mean velocity profiles at four streamwise locations downstream the splitter plate are shown in Fig. 17. In the experiments, the mean velocity profiles from different experimental sections including those close to the splitter plate collapse on the error function shown in Fig. 17d, which is indicative of the boundary layers mixing very close to the plate trailing edge. In the simulations, the mixing is delayed, regardless the time step used. Far away from the splitter plate, the mean velocity profiles obtained with the different time steps are in agreement with the experimental data. Overall, the time step has insignificant effect on the mean velocity evolution.

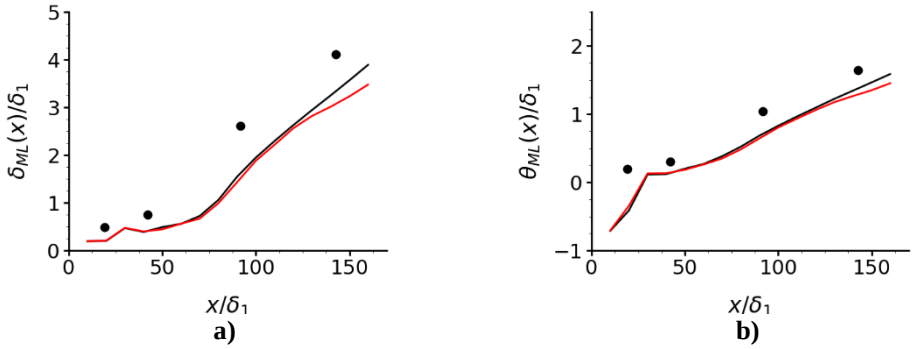

a) **b)**

Fig. 16 The mixing layer growth in Case 1: a) mixing layer thickness, b) mixing layer momentum thickness. Notations: lines - DNS, circles – experiment [18]. Colors: black – $\Delta t_1 = 0.012$, red – $\Delta t_2 = 0.02$.

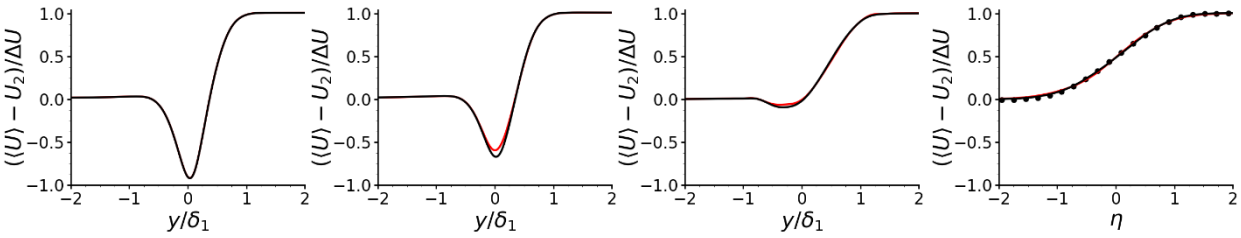

Fig. 17 Mean velocity profiles at different streamwise locations, a) $x/\delta_1 = 10$, b) $x/\delta_1 = 20$, c) $x/\delta_1 = 30$, d) $x/\delta_1 = 160$. Notations are the same as in Fig. 16.

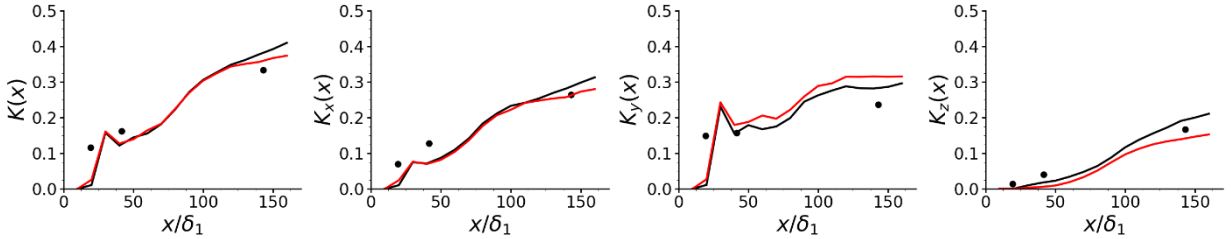

Fig. 18 Streamwise evolution of the turbulent kinetic energy and the normal Reynolds stresses integrated across the mixing layer. Notations are the same as in Fig. 16.

Streamwise evolution of the turbulent kinetic energy and the normal Reynolds stresses, all integrated across the mixing layer, is shown in Fig. 18. Here, the turbulent kinetic energy is defined as $K = 0.5 \cdot (K_x + K_y + K_z)$. The figure demonstrates that transition to turbulence starts at x/δ_1~15 in the simulations with both time steps. That is, the time step does not affect the transition location. In the paper, the starting point of transition to turbulence is associated with $K > 0$. Comparing with the experimental data, transition is delayed, although no exact information about its location is available in [18.24]. This may be due to the experimental boundary layers being turbulent enough before mixing occurs as also seen in Fig. 19 showing the Reynolds stresses.

Influence of the time step on the integrated turbulent kinetic energy and its contribution from the streamwise velocity fluctuations becomes apparent at $x/\delta_1 > 125$. The Reynolds stresses in the transverse and spanwise directions are affected everywhere in the flow: K_y is increased and K_z is reduced in simulations with the larger time step. This indicates that the scales filtered by the larger time step are responsible for the energy transfer to the spanwise velocity fluctuations. In the absence of these scales, the energy is re-directed to velocity fluctuations in the transverse direction. At $x/\delta_1 > 125$, the larger time step leads to reduced energy in velocity fluctuations in both directions tangential to the splitter plate plane: K_x and K_z, and in the turbulent kinetic energy *K*. The effect is beneficial for *K* and K_x when comparing with the experiments, but reduced turbulent kinetic energy may be a cause of the reduced growth of the mixing layer growth seen in Fig. 10 in simulations with Δt_2.

Results for the Reynolds stress profiles are shown in Fig. 19 at $x/\delta_1 = 19.5$, 42, and 143 corresponding to the streamwise locations of experimental stations, and also at $x/\delta_1 = 160$**,** where no experimental data is available. At this location, data from the closest experimental station at $x/\delta_1 = 195$ are used for comparison.

In the simulations, the Reynolds stress in the spanwise direction, $< w^2 >$, is zero at the location $x/\delta_1 = 19.5$, closest to the splitter plate. This is different from the experiments and independent from the simulation time step. The simulation profiles of $< u^2 >$ and $< v^2 >$ also differ from the experimental data in the flow area close to the splitter plate regardless the time step. The maximum values of $< u^2 >$ and $< v^2 >$ are less than in the experiments, where $< v^2 >$ is the largest at this location. This can be attributed to different flow structures in the simulations and the experiments in the vicinity of the splitter plate as discussed above.

The simulation time step affects all non-zero Reynolds stresses, but particularly, $< w^2 >$. A difference in the profiles obtained with different time steps reduces as the mixing layer grows. Results for all Reynolds stresses but $< v^2 >$ tend to agree with the experimental data far downstream from the splitter plate in the simulations with the larger time step. The Reynolds stress in the transverse direction is over-predicted everywhere in the flow with both time steps. A cause of this is currently under investigation.

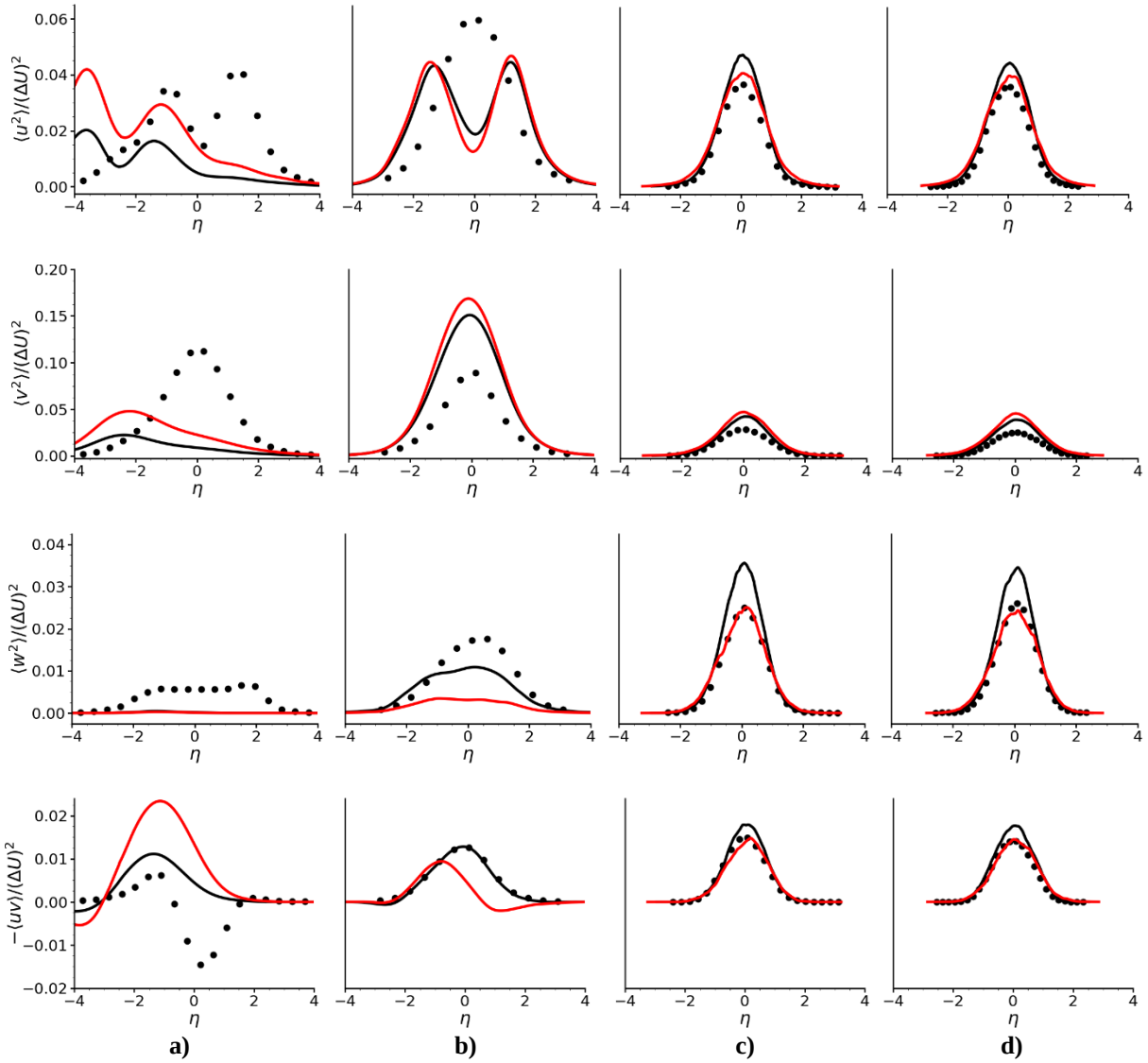

Fig. 19 The Reynolds stresses at different streamwise locations: a) $x/\delta_1 = 19.5$, b) $x/\delta_1 = 42$, c) $x/\delta_1 = 143$, d) $x/\delta_1 = 160$ in simulations and $x/\delta_1 = 195$ in experiments. Notations are the same as in Fig. 16.

Snapshots of instantaneous vortex structures obtained using λ_2-criterion [30] at two different times: $t = 533$ and 2000, are shown in Appendix (Figs. A1 and A2). As the figure demonstrates, variations in the time step affect the flow structure and the mixing layer development. Spanwise vortices appear around the same location, $x/\delta_1 \sim 12$, in the simulations with both time steps, but a process of transitioning to fully-turbulent mixing layer is different. In simulations with Δt_1, the size of vortices in the (x,y)-plane remains almost constant between $x/\delta_1 \sim 40$ and 100. When vortex coupling starts in the simulations with the larger time step, vortices grow gradually. Their vortex structure is also more diffused in the simulations with the smaller time step. Overall, transition to turbulence looks more natural in simulations with Δt_2. A possible explanation could be a numerical origin of scales present in the simulations with the smaller time step, but suppressed in the simulations with the larger time step. This this has to be investigated in more detail.

To summarize, a choice of the time step affects the mixing layer development and its structure. However, its effect on the considered flow characteristics varies. The most affected ones are those relevant to the energy re-distribution in the transverse and spanwise flow directions, with the larger time step suppressing the energy transfer in the spanwise direction and promoting it in the transverse direction. As the mixing layer grows and become fully turbulent, the time step effect on the Reynolds stress profiles diminishes. The total turbulent kinetic energy in the flow is reduced far away from the splitter plate in the simulations with the larger time step.

E. Mixing Layer Inflow Conditions

Simulations for Cases I and II were conducted with $\Delta t = 0.02$ to analyze sensitivity of the mixing layer development to the conditions of the laminar boundary layers at the trailing edge of the splitter plate. In Case II, these conditions are in a better agreement with the experimental data than in the Case I simulations. It means in particular that the boundary layers are faster in Case II.

The mixing layer thickness and its momentum thickness are shown in Fig. 20. In the figure, red lines correspond to Case I and black lines to Case II; symbols are experimental data. Similar notations are used in the following figures of this sub-section. The mixing layer growth rate obtained at $x/\delta_1 > 70$ in Case II is the same as in the experiments. In the area closer to the slitter plate, a difference in the boundary layer conditions in two cases has little effect on the boundary layers mixing, which is slower than in the experiments. The opposite tendency is observed in the mean velocity (Fig. 21). A difference in the boundary layers velocities in Cases I and II is apparent in the splitter plate vicinity, but disappears far downstream from the plate.

Faster boundary layers in the Case II simulations increase the level of the turbulent kinetic energy and all of the normal Reynolds stresses integrated across the mixing layer (Fig. 22). The values of K, K_x, and K_y are also higher than in the experiments everywhere in the flow except at $x/\delta_1 < 20$ in this case. The value of K_z is close to zero in this area and is not affected by the boundary conditions. The transition location to turbulence is also insensitive to considered variations in the boundary layer conditions.

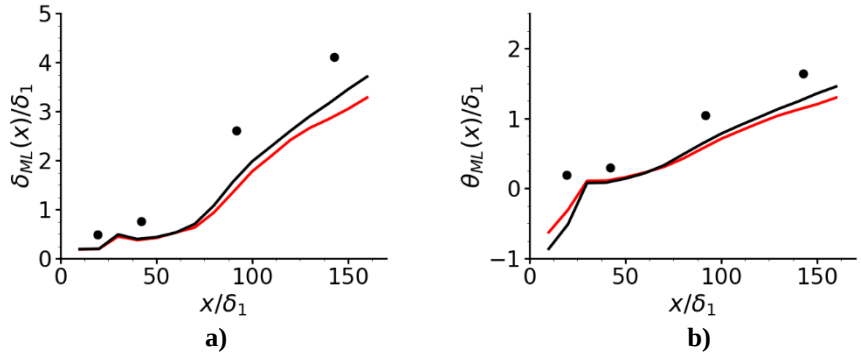

Fig. 20 The mixing layer growth characterized by a) mixing layer thickness, b) momentum thickness. Notations: lines - DNS, circles – experiment [18]. Colors: red – Case I, black – Case II.

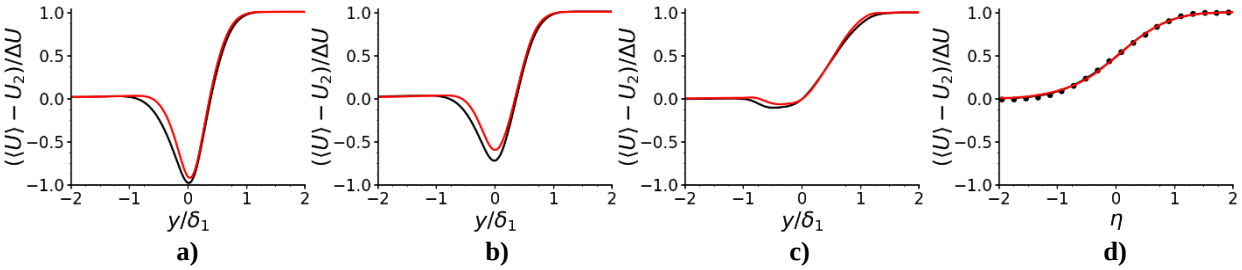

Fig. 21 Mean velocity profiles at different streamwise locations: a) $x/\delta_1 = 10$, b) $x/\delta_1 = 20$, c) $x/\delta_1 = 30$, d) $x/\delta_1 = 160$. Notations are the same as in Fig. 20.

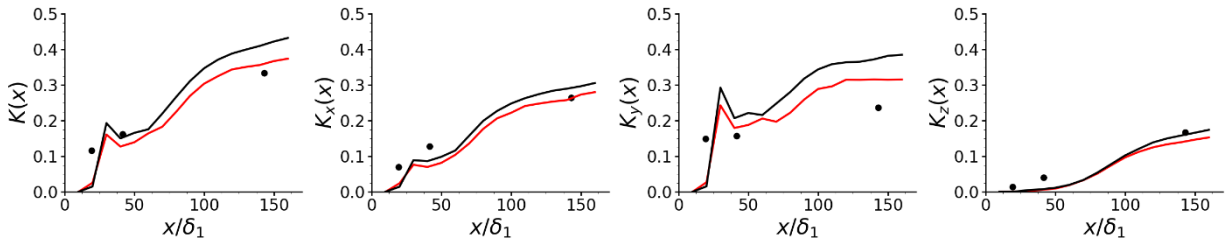

Fig. 22 Streamwise evolution of the turbulent kinetic energy and the normal Reynolds stresses integrated across the mixing layer. Notations are the same as in Fig. 20.

The Reynolds stress profiles are shown in Fig. 23. The figure confirms results for the integrated characteristics presented in Fig. 22. That is, the Reynolds stresses are slightly higher in the Case II simulation everywhere in the flow except for the area closest to the splitter plate. In this area, $x/\delta_1 < 20$, slower boundary layers in Case I mix more efficiently, whereas faster boundary layers in Case II "slip" over each other until they slow down farther downstream. The simulated flow structure obtained in both Cases is different from that of observed in the experimental flow close to the splitter plate. Far away from the splitter plate, the effect from the boundary conditions is still present, but less significant.

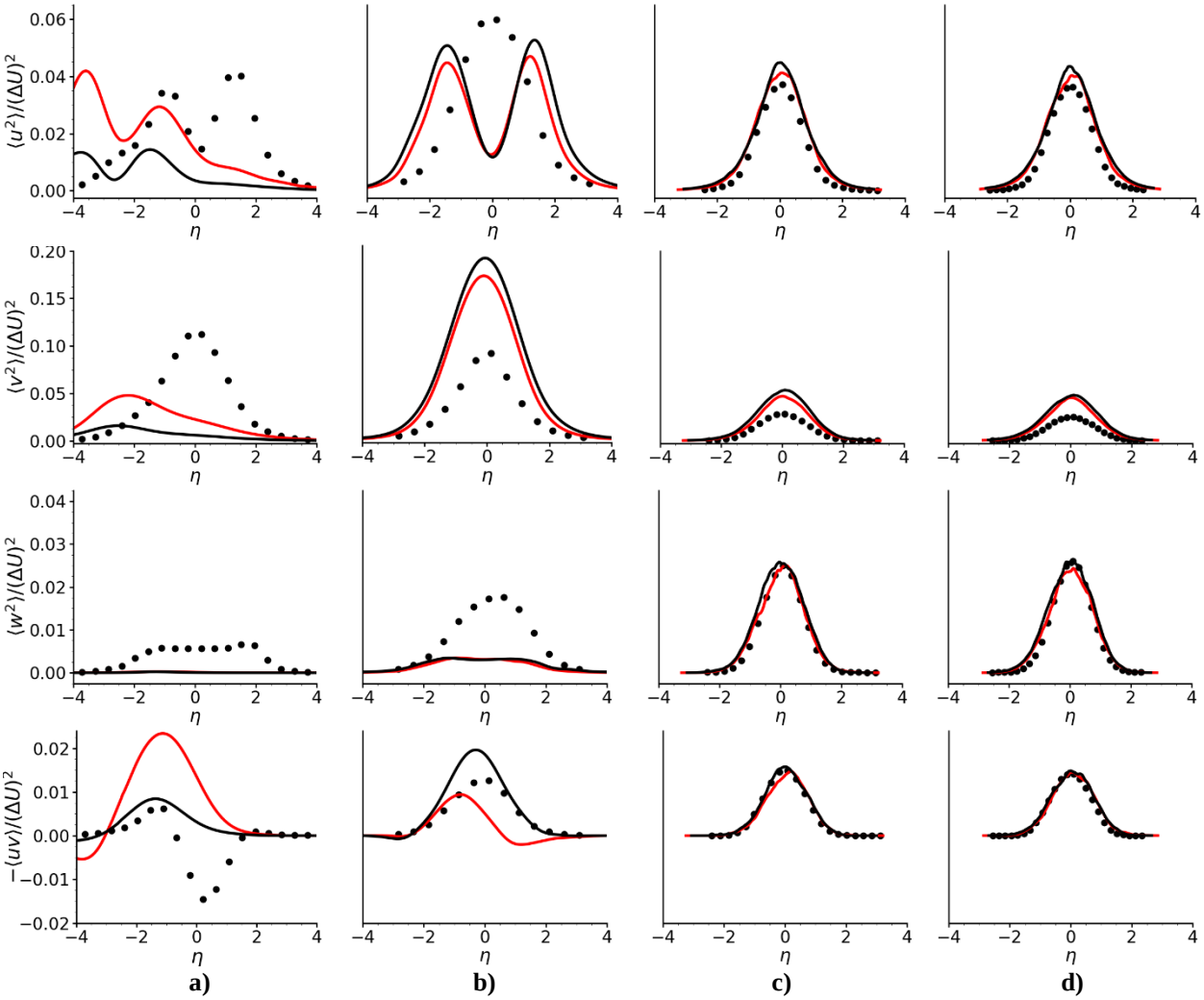

Fig. 23 The Reynolds stresses at different streamwise locations: a) $x/\delta_1 = 19.5$, b) $x/\delta_1 = 42$, c) $x/\delta_1 = 143$, d) $x/\delta_1 = 160$ in simulations and $x/\delta_1 = 195$ in experiments. Notations are the same as in Fig. 20.

F. Domain Transverse Dimension

In the experiments, the test section was $90\delta_1$ in the transverse direction bounded by a solid wall at one side and by a flexible wall at the other. To avoid resolving the development of boundary layers on these walls in simulations, the walls are not modeled in the simulations, while the initial domain size in this direction, L_y, was set to $70\delta_1$ ($\pm 35\delta_1$). To assess sensitivity of the simulation results to variations in this parameter, simulations were conducted using domains with reduced and increased dimensions in this direction: $50\delta_1$ ($\pm 25\delta_1$) and $90\delta_1$ ($\pm 45\delta_1$), respectively (Case III and Case IV as compared to Case II).. Other domain dimensions and the time step ($\Delta t = 0.02$) used in these simulations are the same for Cases II-IV. The grid of the same resolution is used in all simulations, with its minor modification for Cases III and IV as described in Section III D.

Cases III and IV started from the Case II solution at $t = 500$ after the transient period has passed to reduce the simulation cost. To maximize the number of samples used for the data averaging, a presence of the transient period in solutions for Cases III and IV was neglected after reviewing the solutions time evolution in Fig. 8 which shows essentially similar behavior of volume-averaged statistics after $t = 500$ in all three cases. The lack of sensitivity in volume-averaged quantities does not mean that the local flow characteristics are not affected by a potential transient. This is an additional source of uncertainty in simulations for these two cases to compare with Case II, but the same uncertainty source in both. In this regard, results from the Case II simulations should be viewed only as a reference in Figs. 24-27 without expectation to be closely matched. In the figures, black, red, and blue lines correspond to Cases II, III, and IV respectively; experimental data are shown by circles.

The figures demonstrate that the parameters relevant to the mixing layer growth (Fig. 24), mean velocity profiles (Fig. 25), and the transition location (Fig. 26) are insensitive to this domain dimension variation. Differences observed in the streamwise evolution of the turbulent kinetic energy and its contributions in different directions integrated across the mixing layer are insignificant (Fig. 26) and may be attributed to the data quality.

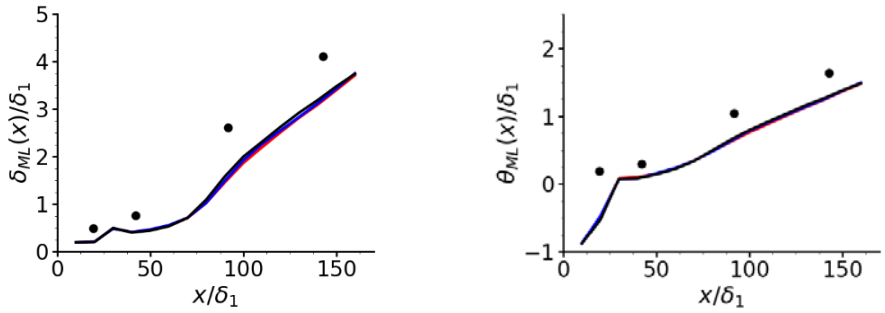

a) **b)**

Fig. 24 The mixing layer growth characterized by a) mixing layer thickness, b) momentum thickness. Notations: lines - DNS, circles – experiment [18]. Colors: Black – Case II, red – Case III, blue – Case IV.

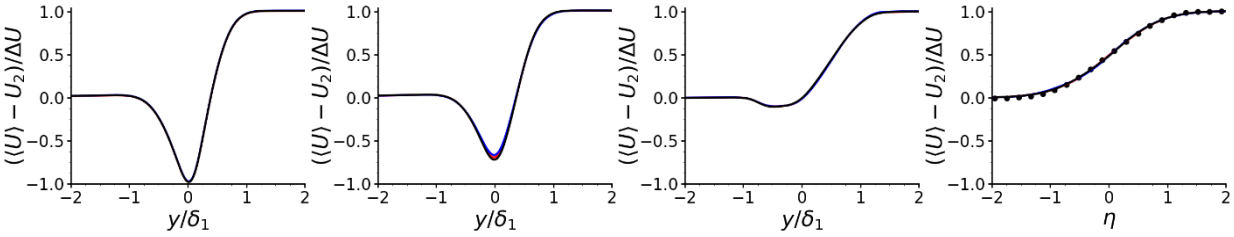

a) **b)** **c)** **d)**

Fig. 25 Mean velocity profiles at different streamwise locations: a) $x/\delta_1 = 10$, b) $x/\delta_1 = 20$, c) $x/\delta_1 = 30$, d) $x/\delta_1 = 160$. Notations are the same as in Fig. 24.

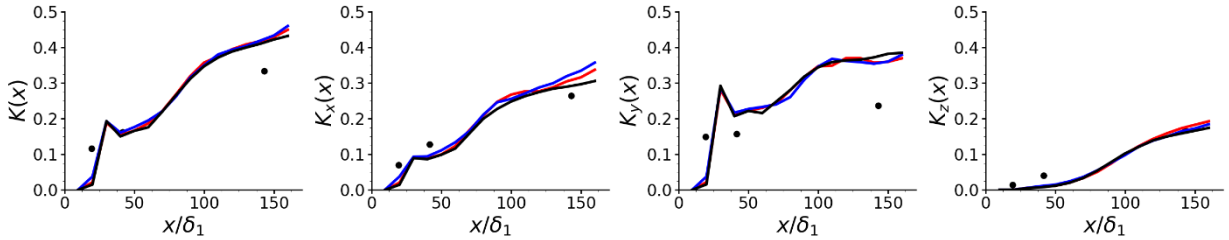

Fig. 26 Streamwise evolution of the turbulent kinetic energy and the normal Reynolds stresses integrated across the mixing layer. Notations are the same as in Fig. 24.

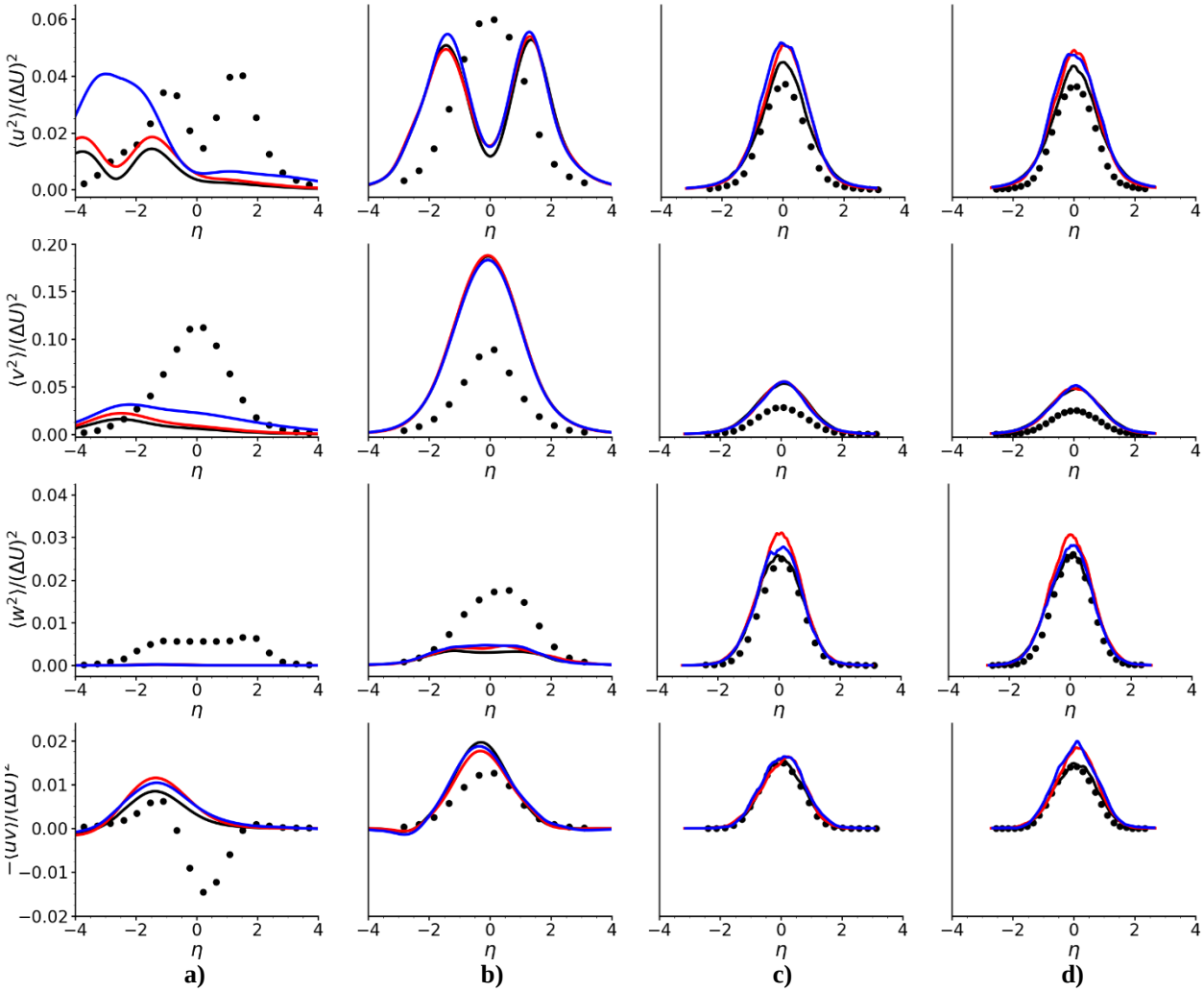

Fig. 27 The Reynolds stresses at different streamwise locations: a) $x/\delta_1 = 19.5$, b) $x/\delta_1 = 42$, c) $x/\delta_1 = 143$, d) $x/\delta_1 = 160$ in simulations and $x/\delta_1 = 195$ in experiments. Notations are the same as in Fig. 24.

Substantial difference in the solutions is observed in the profiles of the normal Reynolds stresses (Fig. 27). Specifically, profiles for $< u^2 >$ and $< v^2 >$ in the splitter plate vicinity are higher in the largest domain (Case IV) than in the other two cases, and the shape of these profiles suggests that the solution may not yet be sufficiently converged in this flow area. That is, this effect is unlikely to be due to the domain transverse dimension and may be eliminated with running simulations longer. On the other hand, the increase in the Reynolds stress in the spanwise direction, $< w^2 >$, far downstream from the splitter plate with reducing the domain size in the thansverse direction can be linked to variations in this domain dimension. However, considering changes in all flow characteristics presented in Figs. 24-27, even this effect is not significant.

Overall, the results presented in Figs. 24-27 indicate that the simulations results are essentially insensitive to considered variations in the domain transverse dimension. This is in agreement with the criterion on this domain dimension, $6.96 < L_y/\delta_{\omega,max} < 8.3$, proposed in [25,26], because even the smallest domain in this direction used in the current study has $L_y/\delta_{\omega,max} = 8.03$. For practical purposes, the lower bound of this criterion should be investigated more thoroughly.

G. Domain Streamwise Dimension

To analyze the effect of the domain streamwise dimension on the mixing layer development, two cases were considered with the different lengths of the mixing layer region: $L_x = 350\delta_1$ (Case V) and $170\delta_1$ (Case VI). The domain outlet location for these cases is $x/\delta_1 = 350$ and 170, respectively. The grid shown in Fig. 6b was used in the simulations for these cases. The time step and simulation time are the same in both cases: $\Delta t = 0.02$ and $t = [0,2000]$

with statistics collected in the interval of $[500, 2000]$, but with less frequency in Case V, due to increased data storage requirements. That is less flow fields are available for the data averaging in Case V, which is an additional source of uncertainty when comparing the results of these simulations. This may influence the flow characteristics relevant to the energy re-distribution between the transverse and spanwise directions, with more energy being distributed to $< v^2 >$ and less to $< w^2 >$ when running the Case V simulations longer. Other parameters are not expected to change significantly as shown in Figs. 11-15.

Parameters characterizing the mixing layer growth are shown in Fig. 28. Red and black lines correspond to Cases V and VI in the figure; symbols are experimental data. As the figure demonstrates, the effect from increasing the mixing layer region length is substantial. The mixing layer growth is suppressed in the flow area $x/\delta_1 < 170$ in Case V. In Case VI, velocity deficit from the wake effect of the splitter plate vanishes more rapidly than in Case V, even though both cases produce the typical mixing layer mean velocity profile downstream (Fig. 29). That is, the laminar boundary layers in Case V penetrate farther downstream than in Case VI, delaying the development of the mixing layer.

Transition to turbulence is also delayed as seen in Fig. 30: $x/\delta_1 \approx 25$ in Case V and $x/\delta_1 \approx 15$ in Case VI. Once transition started, the normal Reynolds stresses integrated across the mixing layer, K_x and K_y, and the turbulent kinetic energy, K, grow rapidly in Case V, exceeding their values from Case VI at $x/\delta_1 > 100$ (Fig. 30). The growth rate of K_z is not affected by variations in the mixing layer region length.

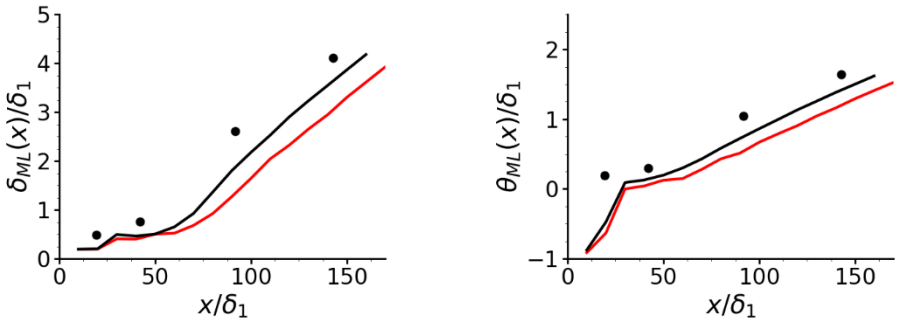

Fig. 28 The mixing layer growth characterized by a) mixing layer thickness, b) momentum thickness. Notations: lines - DNS, circles – experiment [18]. Colors: red – Case V, black – Case VI.

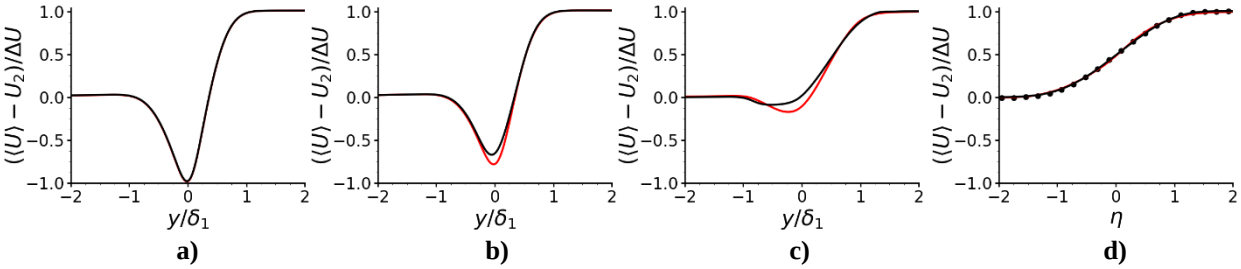

Fig. 29 Mean velocity profiles at different streamwise locations: a) $x/\delta_1 = 10$, b) $x/\delta_1 = 20$, c) $x/\delta_1 = 30$, d) $x/\delta_1 = 160$. Notations are the same as in Fig. 28.

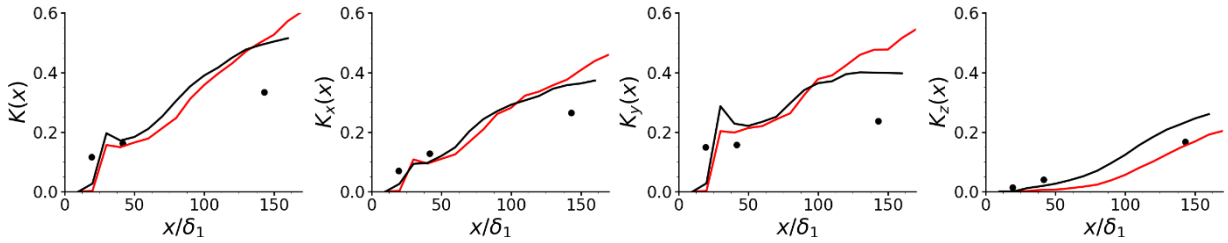

Fig. 30 Streamwise evolution of the turbulent kinetic energy and the normal Reynolds stresses integrated across the mixing layer. Notations are the same as in Fig. 28.

The Reynolds stress profiles shown in Fig. 31 confirm conclusions made from the results presented in Fig. 28-30, that the mixing of the boundary layers is delayed in Case V, but far away from the splitter plate, the normal Reynolds stresses in the (*x*, *y*)-plane are higher in Case V than those in Case VI.

Flow visualization of instantaneous vortex structures is shown for Case V in Fig. A3 at two different times: $t = 1100$ and 2000, using iso-surfaces of λ_2-criterion. The simulated flow in this case has different structure from those in Figs. A1 and A2 confirming that turbulence is still under development at $x/\delta_1 < 170$. Visualization for Case VI is currently in progress and will be discussed during the presentation.

A cause of the strong effect that the mixing layer region length has on simulations requires further clarification. It can be of numerical or physical origin or a combination of both. The imposed outlet conditions may alter the mixing layer development. Strong influence of the domain streamwise dimension on the mixing layer was also observed in the experiments [31]. In [31], it was suggested that large vortex structures near the experimental outlet boundary may be coupled to small structures upstream, producing a feedback mechanism between upstream and downstream flows. This makes the mixing layer structure and development dependent on the streamwise size of the experimental test section. Implications of existence of such a correlation for simulations of a spatially developing mixing layer have yet to be fully comprehended particularly, with respect to the analysis of its self-similar regime.

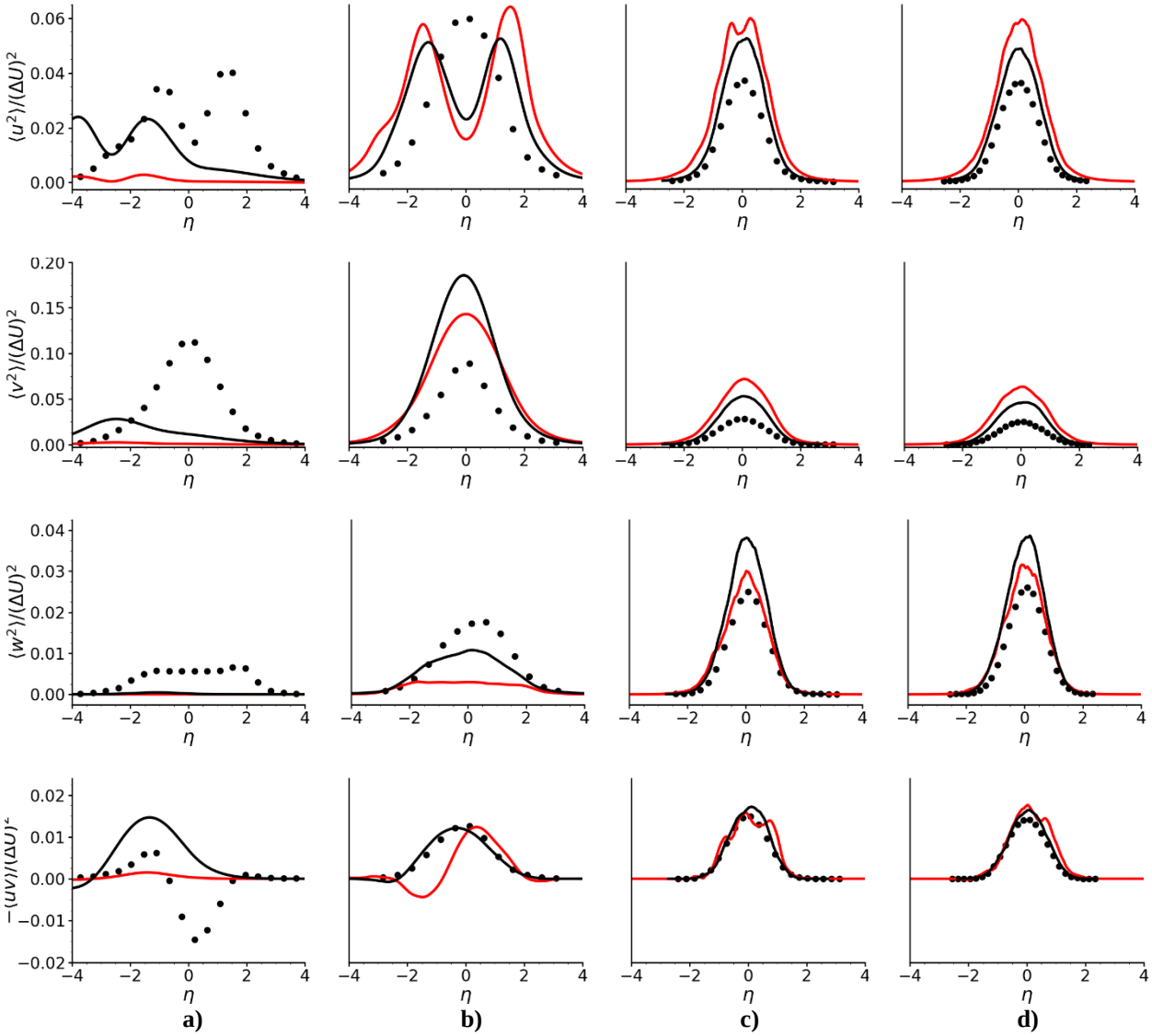

Fig. 31 The Reynolds stresses at different streamwise locations: a) $x/\delta_1 = 19.5$, b) $x/\delta_1 = 42$, c) $x/\delta_1 = 143$, d) $x/\delta_1 = 160$ in simulations and $x/\delta_1 = 195$ in experiments. Notations are the same as in Fig. 28.

H. On the Grid Resolution Effects

Cases IV and VI have the same dimensions in the (*x*, *y*)-plane, but use different grids, with the finer grid being used in Case VI. There are other differences as well between these cases, which complicates using these cases for the grid sensitivity analysis. In particular, the cases have different domain dimensions in the spanwise direction: $23.4\delta_1$ in Case IV and $40\delta_1$ in Case VI. Statistics were collected during the same time, but the Case IV simulations started from the Case II solution at $t = 500$, with the transient period data being used in calculating statistics. That is, there are three major sources of uncertainties to take into account when comparing solutions from these two cases.

On the other hand, some information on the grid resolution effects still can be extracted from comparing Cases IV and VI. This is because the effect of variations of the spanwise domain dimension have already been analyzed in [14] in simulations with the infinitely thin splitter plate, where it was found that the increase in the domain spanwise dimension shifts the transition location to turbulence upstream, facilitates the mixing layer growth, increases K_z and the Reynolds stress $< w^2 >$ far away from the plate. It also leads to reduced values of K, K_x, and K_y everywhere in the flow and $< uv >$ far away from the plate. Interestingly, no substantial effect on the profiles of $< u^2 >$ and $< v^2 >$ has been detected, when varying this simulation parameter. Consequences of including the transient period data in calculating statistics were discussed in Section IV F. This leads to over-predicting $< u^2 >$ everywhere in the mixing layer and K_x and $< uv >$ far away from the plate when comparing Case IV to Case II. Other considered flow characteristics remain largely unaffected by this process. That is, these two sources of uncertainty tend either counteract each other or not interfere. Taking into account this information, comparing Cases IV and VI can be useful for understanding the grid resolution effects.

Figure 32 show parameters that characterize the mixing layer growth obtained in these cases. The increase of these parameters in Case VI is consistent with the results from [14] and is most likely driven by the increased spanwise domain dimension. The mean velocity profiles (Fig. 33) are the same in Cases IV and VI regardless differencese in the simulations. The same can be said about the transition location to turbulence (Fig. 34). In [14], the transition location was shifted in simulations with the infinitely thin splitter plate, when the domain spanwise dimension varied, but not when the plate thickness changed. Thus, the grid resolution may contribute in fixing the transition start point at the same location in Cases IV and VI.

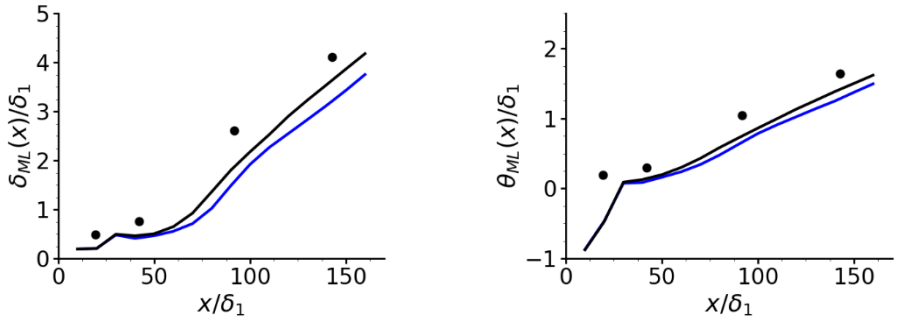

a) **b)**

Fig. 32 The mixing layer growth characterized by a) mixing layer thickness, b) momentum thickness. Notations: lines - DNS, circles – experiment [18]. Colors: Blue – Case IV, black – Case VI.

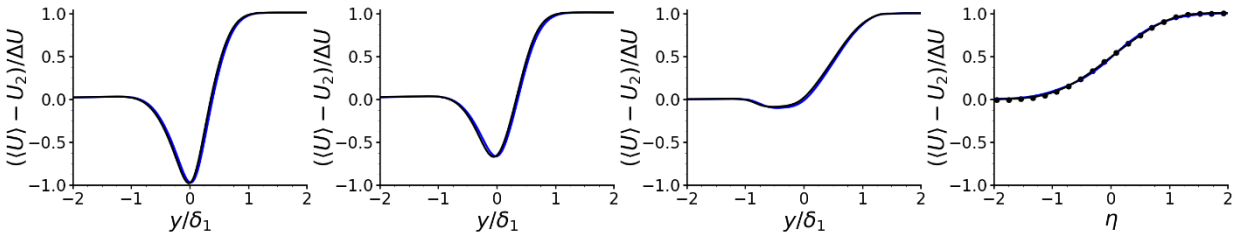

a) **b)** **c)** **d)**

Fig. 33 Mean velocity profiles at different streamwise locations: a) $x/\delta_1 = 10$, b) $x/\delta_1 = 20$, c) $x/\delta_1 = 30$, d) $x/\delta_1 = 160$. Notations are the same as in Fig. 32.

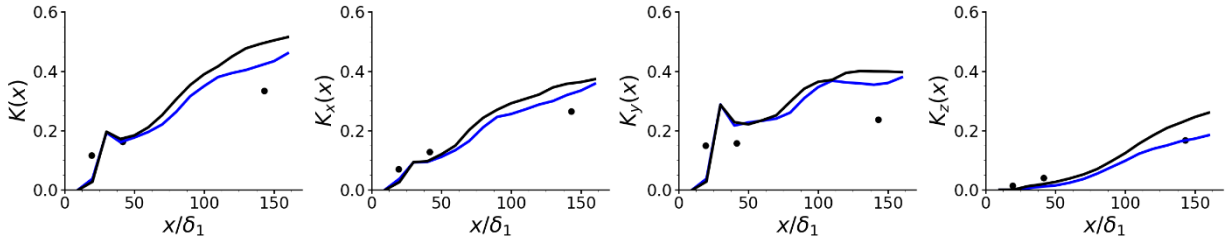

Fig. 34 Streamwise evolution of the turbulent kinetic energy and the normal Reynolds stresses integrated across the mixing layer. Notations are the same as in Fig. 32.

The integrated turbulent kinetic energy and normal Reynolds stresses were also strongly affected by the domain spanwise dimension in [14], but not by the plate thickness. In Cases IV and VI, they vary (Fig. 34), but the observed tendencies are opposite to those reported in [14] for K, K_x, and K_y, that is, these parameters are increased in Case VI to compare with Case IV. Therefore, we can infer that differences between the two cases for these parameters are likely due to the grid resolution. The change in K_z can be caused by the increase in both, the domain spanwise dimension and the grid resolution.

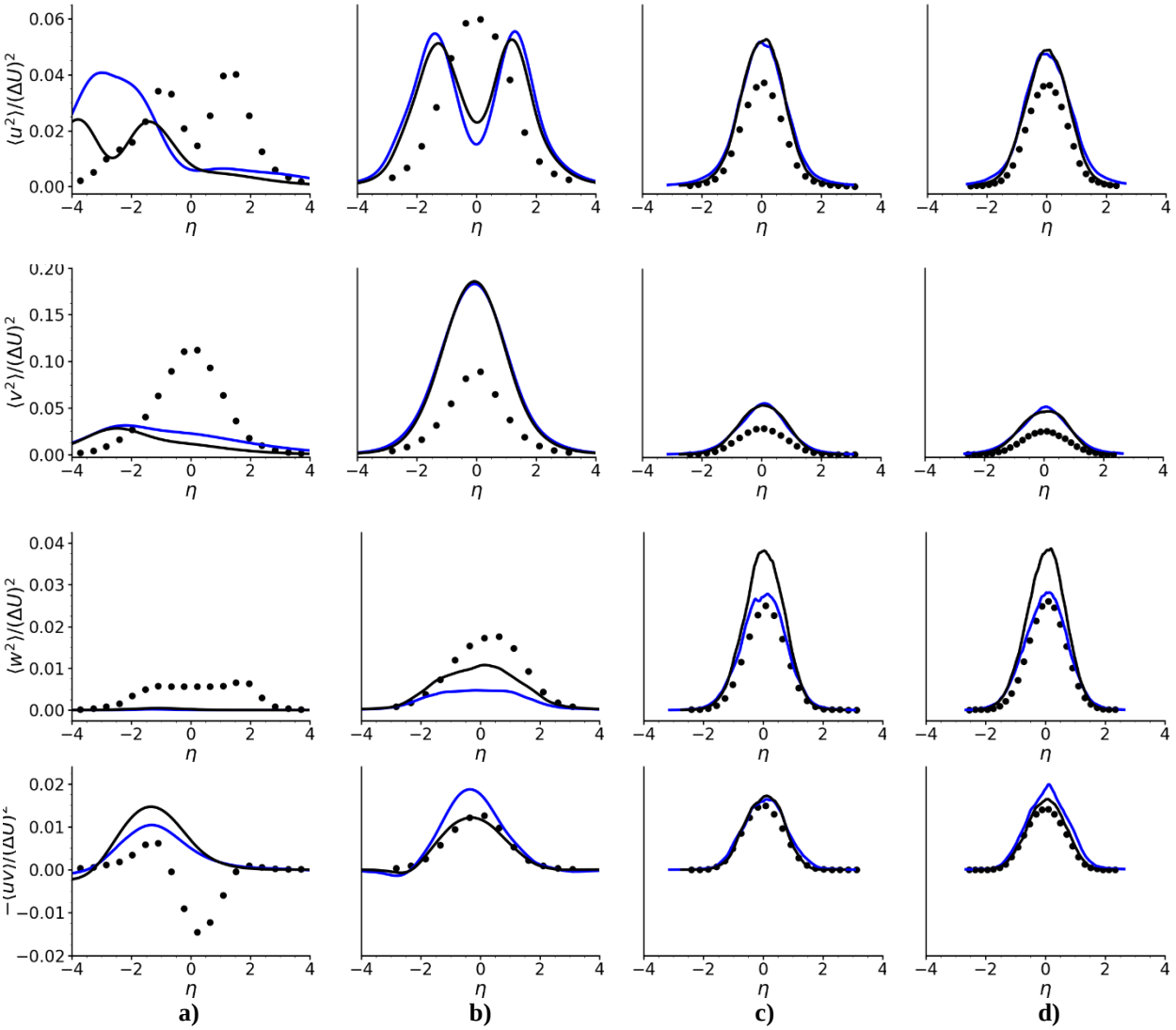

Fig. 35 The Reynolds stresses at different streamwise locations: a) $x/\delta_1 = 19.5$, b) $x/\delta_1 = 42$, c) $x/\delta_1 = 143$, d) $x/\delta_1 = 160$ in simulations and $x/\delta_1 = 195$ in experiments. Notations are the same as in Fig. 32.

The Reynolds stress profiles obtained in Cases IV and VI are shown in Fig. 35. Variations in the $< w^2 >$-profile observed in the two cases are consistent with those reported in [14] when the domain spanwise dimension varied. It does not exclude the grid resolution effect though. The grid resolution is the main factor in variations of $< u^2 >$, $< v^2 >$, and $< uv >$ at the location closest to the splitter plate. The effect on $< uv >$ continues farther downstream. Far away from the plate, the Reynolds stresses in the (*x, y*)-plane are only weakly affected by the differences in the two cases.

Notice also that the differences in simulations, including the use of a finer grid in Case VI does not affect the structure of the boundary layers and how they mix in the plate vicinity. That is, characteristics of the simulated flows in both cases are different from those of the experimental flow in the splitter plate vicinity. Only far away from the plate, simulated and experimental flows exhibit similarity.

V.Conclusions

The paper presented results of DNS of a planar spatially developing turbulent mixing layer between two co-flowing laminar boundary layers. The flow conditions were specified to closely match the experimental ones [18,24] where nominally laminar boundary layers were formed on the opposite sides of the splitter plate before mixing. The sharp-ended splitter plate was used in the simulations and in the experiments, with the plate being of uniform thickness in the simulations, but tapered in the experiments. The plate thickness at the trailing edge was the same in the experiments and in the simulations.

The purpose of conducted simulations was to understand sensitivity of the simulation results to variations in certain simulation parameters. Parameters considered in the paper were the time step in a temporal discretization scheme, boundary layer characteristics at the trailing edge of the splitter plate, and dimensions of the computational domain in the transverse and streamwise flow directions. No artificially generated perturbations were seeded into the flow to eliminate uncertainty in the simulation results associated with such a procedure.

Qualitative analysis was conducted to determine the optimal combination of simulation parameters for cost-effective, but accurate DNS of a spatially developing mixing layer capable to achieve the flow self-similarity within the computational domain.

Six computational domains of similar geometry, but different dimensions were used in simulations. Two grid topologies were generated, with one of them having finer resolution in the plate wake and the mixing layer area. These grids were minimally modified as required without affecting their resolution. No focused grid sensitivity analysis was conducted, but some observations were reported. For example, the grid resolution predictably affects the Reynolds stresses in the vicinity of the splitter plate, but not the mixing layer growth in this flow area and the initial transition location to turbulence. The grid resolution influence diminishes far downstream from the plate.

A choice of the time step predictably affects the mixing layer development and its structure. However, not all flow characteristics were found to be sensitive to this parameter. This includes the initial location of transition to turbulence and the mixing layer growth, which is only affected far away from the splitter plate. The most affected statistics are those relevant to the energy re-distribution in the transverse and spanwise flow directions and particularly, $< w^2 >$, which is suppressed by the increase in the time step. As the mixing layer grows and become fully turbulent, the time step effects on the Reynolds stresses diminishes, with the turbulent kinetic energy in the flow being reduced far away from the splitter plate in the simulations with the larger time step.

Conditions of the boundary layers at the trailing edge of the splitter plate also have different effect on different mixing layer characteristics. The transition location to turbulence, initial growth rate of the mixing layer, and the integrated characteristics close to the splitter plate are insensitive to considered variations in the boundary layer conditions. Far downstream from the splitter plate, faster boundary layers contribute to increase of the turbulent kinetic energy particularly, in the (*x,y*)-plane and in the transverse direction. Matching in simulations the experimental boundary layer conditions leads to the mixing layer growth in agreement with the experiments far away from the splitter plate. The effect on the mean flow velocity and all the Reynolds stresses except for $< w^2 >$ is stronger in the near plate area. That is, slower boundary layers mix more intensively in the (*x,y*)-plane.

The effect from variations in the domain transverse dimension was found negligible in our simulations in agreement with the criterion on this domain dimension, $6.96 < L_y/\delta_{\omega,max} < 8.3$, proposed in [25,26]. The smallest domain in this direction used in the current study had $L_y/\delta_{\omega,max} = 8.03$. For practical purposes, the lower bound of this criterion should be investigated more thoroughly.

On the other hand, the increase of the domain streamwise dimension, so that the mixing layer region length is increased, has a strong effect on the mixing layer development and structure. In particular, the mixing layer growth is suppressed and transition to turbulence is delayed in the considered flow area $x/\delta_1 < 170$ in the longer domain.

However, the turbulent kinetic energy accumulated in the (x,y)-plane of the flow by this location is higher when the domain length is increased. A cause of this phenomenon and its implications for the spatially developing mixing layer simulations has yet to be fully comprehended.

Acknowledgments

Resources supporting this work were provided by the NASA High-End Computing (HEC) Program through the NASA Advanced Supercomputing (NAS) Division at Ames Research Center. Flow visualization using FieldView software was possible thanks to Intelligent Light who provided an academic license. Dr. S. V. Poroseva acknowledges partial support from the DTRA Grant HDTRA1-18-1-0022.

References

[1] Weller, H. G., Tabor, G., Gosman, A. D., Fureby, C., "Application of a Flame-Wrinkling LES Combustion Model to a Turbulent Mixing Layer," *Symposium (Intl.) on Combustion*, 1998, Vol. 27, No. 1, pp. 899-907.

[2] Yoder, D., Debones, J., and Georgiadis, N, "Modeling of Turbulent Free Shear Flows," *Computers & Fluids*, Vol. 117, 2015, pp. 212-232.

[3] Oberkampf, W. L., Roy, C. J. *Verification and Validation in Scientific Computing*, Cambridge University Press; 1 edition, 2010.

[4] T. J. Barth, "An overview of combined uncertainty and a posteriori error bound estimates for CFD calculations," *46th AIAA Fluid Dynamics Conference, AIAA AVIATION Forum*, AIAA 2016–1062.

[5] Poroseva, S. V., Colmenares F., J. D., and Murman, S. M., "On the accuracy of RANS simulations with DNS data," *Phys. Fluids*, Vol. 28, No. 11, 2016, pp. 115102-1.

[6] Mansour, N. N., Kim, J., and Moin, P., "Reynolds-stress and dissipation-rate budgets in a turbulent channel flow," *J. Fluid Mech*., Vol. 194, 1988, pp. 15-44.

[7] Hoyas, S., and Jiménez, J., "Reynolds Number Effects on the Reynolds-stress Budgets in Turbulent Channels," *Phys. Fluids*, Vol. 20, 2008, pp. 100511-1.

[8] Oliver, T. A., Malaya, N., Ulerich, R., and Moser, R. D., "Estimating uncertainties in statistics computed from direct numerical simulation," *Phys. Fluids*, Vol. 26, No. 3, 2014, pp. 035101-1.

[9] Lee, M., and Moser, R. D., "Direct numerical simulation of turbulent channel flow up to $Re_\tau = 5200$," *J. Fluid Mech.*, Vol. 774, 2015, pp. 395-415.

[10] Jeyapaul, E., Coleman, G. N., and Rumsey, C. L., "Higher-order and length-scale statistics from DNS of a decelerated planar wall-bounded turbulent flow," *Int. J. Heat Fluid Flow*, 2015, Vol. 54, 14–27 (2015).

[11] Sillero, J. A., Jiménez, J., and Moser, R. D., "One-Point Statistics for Turbulent Wall-Bounded Flows at Reynolds Numbers up to $\delta^+ \approx 2000$," *Phys. Fluids*, Vol. 25, 2013, pp. 105102.

[12] Poroseva, S. V., Jeyapaul, E., Murman, S. M., and Colmenares F., J. D., "The Effect of the DNS Data Averaging Time on the Accuracy of RANS-DNS Simulations," *46th AIAA Fluid Dynamics Conference, AIAA AVIATION Forum*, AIAA 2016-3940.

[13] Poroseva, S. V., Kaiser, B. E., Sillero, J. A., Murman, S. M., "Validation of a Closing Procedure for Fourth-Order RANS Turbulence Models with DNS Data in an Incompressible Zero-Pressure-Gradient Turbulent Boundary Layer," *Int. J. Heat and Fluid Flow*, 2015, Vol. 56, pp. 71-79.

[14] Colmenares F., J.D., Poroseva, S.V., Peet, Y.T., and Murman, S.M., "DNS of a Spatially Developing Turbulent Mixing Layer from Co-flowing Laminar Boundary Layers", *47th AIAA Fluid Dynamics Conference, AIAA AVIATION Forum*, AIAA 2017-3641.

[15] Ko, J., Lucor, D., and Sagaut, P., "Sensitivity of two-dimensional spatially developing mixing layers with respect to uncertain inflow conditions," *Phys. Fluids*, Vol. 20, No. 7, 2008, pp. 077102-1.

[16] Moser, R. D., and Rogers, M., "The three-dimensional evolution of a plane mixing layer: Pairing and transition to turbulence," *J. Fluid Mech.*, Vol. 247, 1993, pp. 275-320.

[17] Laizet, S., Lardeau, S., and Lamballais, E., "Direct numerical simulation of a mixing layer downstream a thick splitter plate." *Phys. Fluids*, Vol. 22, No. 1, 2010, pp. 015104-1.

[18] Bell, J. H., and Mehta, R. D., "Development of a two-stream mixing layer from tripped and untripped boundary layers," *AIAA Journal*, Vol. 28, No. 12, 1990, pp. 2034-2042.

[19] A. T. Patera, "A spectral element method for fluid dynamics: laminar flow in a channel expansion," *Journal of Computational Physics*, Vol. 54, 1984, pp. 468–488.

[20] Fischer, P., Kruse, J., Mullen, J., Tufo, H., Lottes, J. & Kerkemeier, S., "NEK5000: Open source spectral element CFD solver," 2008. URL: https://nek5000.mcs.anl.gov

[21] Deville, M. O.; Fischer, P. F.; Mund, E. H. *High-Order Methods for Incompressible Fluid Flow*; Cambridge Monographs on Applied and Computational Mathematics, 9; Cambridge University Press: Cambridge, UK, 2002.

[22] Karniadakis, G., Israeli, M., and Orszag, S., "High-order splitting methods for the incompressible Navier-stokes equations," *J. Comput. Phys*, Vol. 97, No. 2, 1991, pp. 414–443.

[23] Maday, Y., Patera, A.T. and Rønquist, E.M., "An Operator-integration-factor splitting method for time-dependent problems: Application to incompressible fluid flow", J. Sci. Comput., Vol. 5, No. 4, 1990, pp 263–292. doi: 10.1007/BF01063118

[24] Bell, J. H., and Mehta, R. D., “Design and calibration of the mixing layer and wind tunnel,” JIAA TR-89, Department of Aeronautics and Astronautics, Stanford University, Stanford, CA, 1989
[25] Wang, Y., Tanahashi, M., and Miyauchi, T., “Coherent fine scale eddies in turbulence transition of spatially-developing mixing layer,” *Intl. Journal of Heat and Fluid Flow*, Vol. 28, 2007, pp. 1280-1290.
[26] Attili, A., and Bisetti, F., “Statistics and scaling of turbulence in a spatially developing mixing layer at Reλ= 250,” *Phys. Fluids*, Vol. 24, No. 3, 2012, 035109.
[27] McMullan, W. A., “Spanwise Domain Effects on the Evolution of the Plane Turbulent Mixing Layer,” *Int. J. Computational Fluid Dynamics*, Vol 29, Nos. 6–8, 2015, pp. 333–345.
[28] Ohlsson, J., Schlatter, P., Fischer, P. F., and Henningson, D. S., “Direct numerical simulation of separated flow in a three-dimensional diffuser,” *J. Fluid Mech*., Vol. 650, 2010, pp. 307.
[29] Vinuesa, R., Hosseini, S. M., Hanifi, A., Henningson, D. S., and Schlatter, P., “Direct numerical simulation of the flow around a wing section using high-order parallel spectral methods,” *Intl. Symp. on Turbulence and Shear Flow Phenomena*, January, 2015, pp. 1-6.
[30] Jeong, J, and Hussain, F., "On the Identification of a Vortex," *Journal of Fluid Mechanics*, Vol. 285, 1995, pp. 69-94.
[31] Dimotakis, P. E., and Brown, G. L., “The Mixing Layer at High Reynolds Number: Large-Structure Dynamics and Entrainment”, *Journal of Fluid Mechanics*, Vol. 78, No. 3, 1976, pp. 535.

Appendix

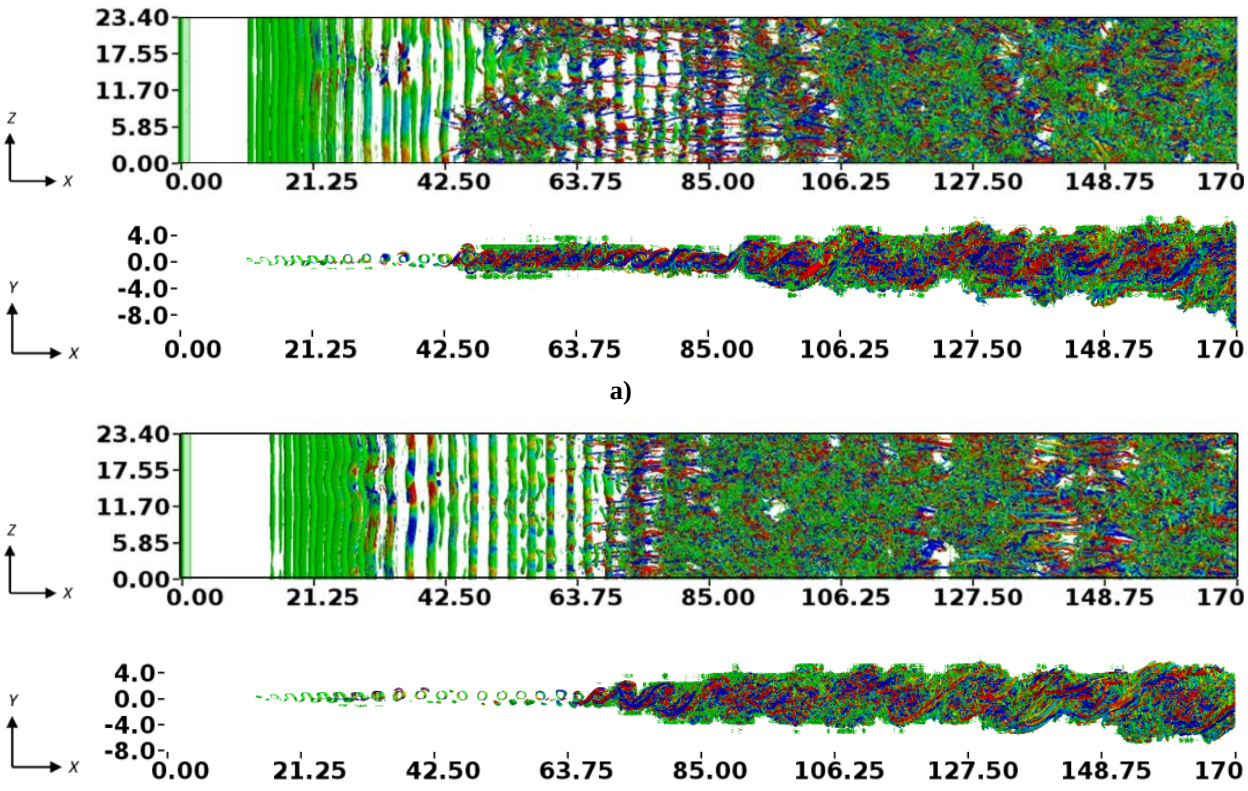

a)

b)

Fig. A1 Plan and side views of vortex structures obtained in the Case I simulations at $t = 533$ using iso-surfaces at $\lambda_2 = -0.001$: a) simulations with the time step Δt_1 , b) simulations with the time step Δt_2. Color scheme: green – $\omega_x \approx 0$, blue – $\omega_x < 0$, red – $\omega_x > 0$. All axes are normalized with δ_1.

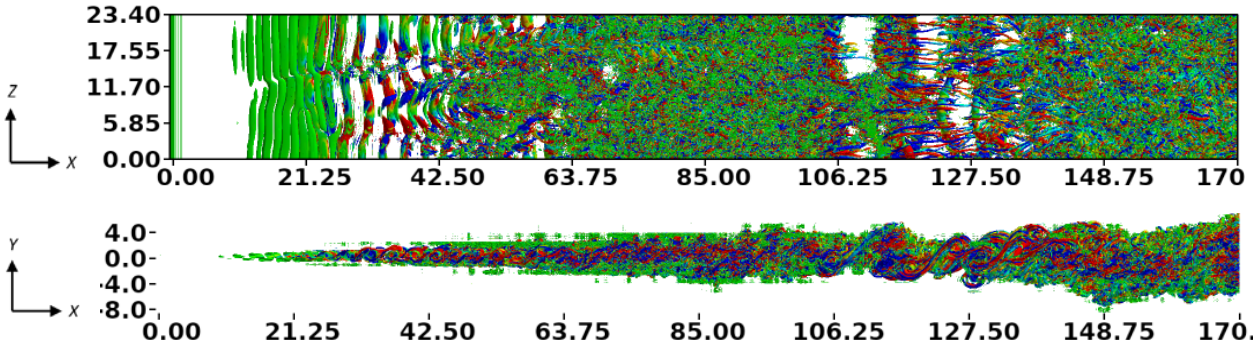

a)

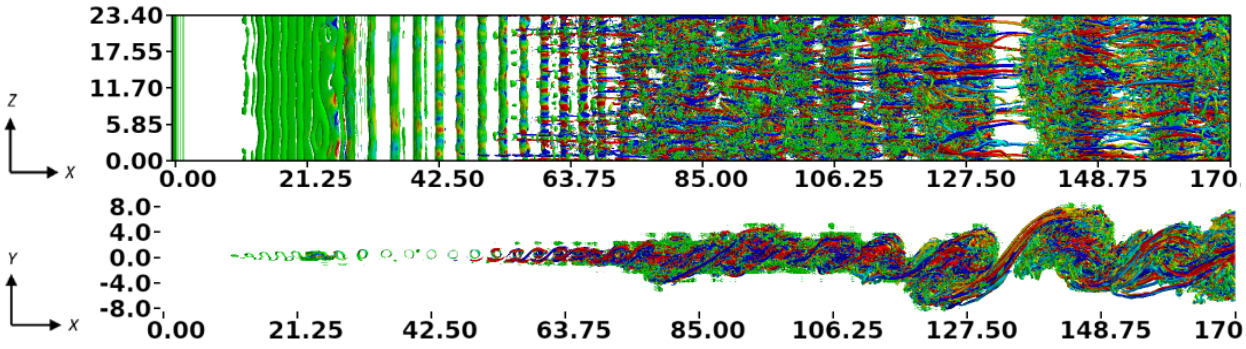

b)

Fig. A2 Plan and side views of vortex structures obtained in the Case I simulations at $t = 2000$ using iso-surfaces at $\lambda_2 = -0.001$: a) simulations with the time step Δt_1 , b) simulations with the time step Δt_2. Notations are the same as in Fig. A2. All axes are normalized with δ_1.

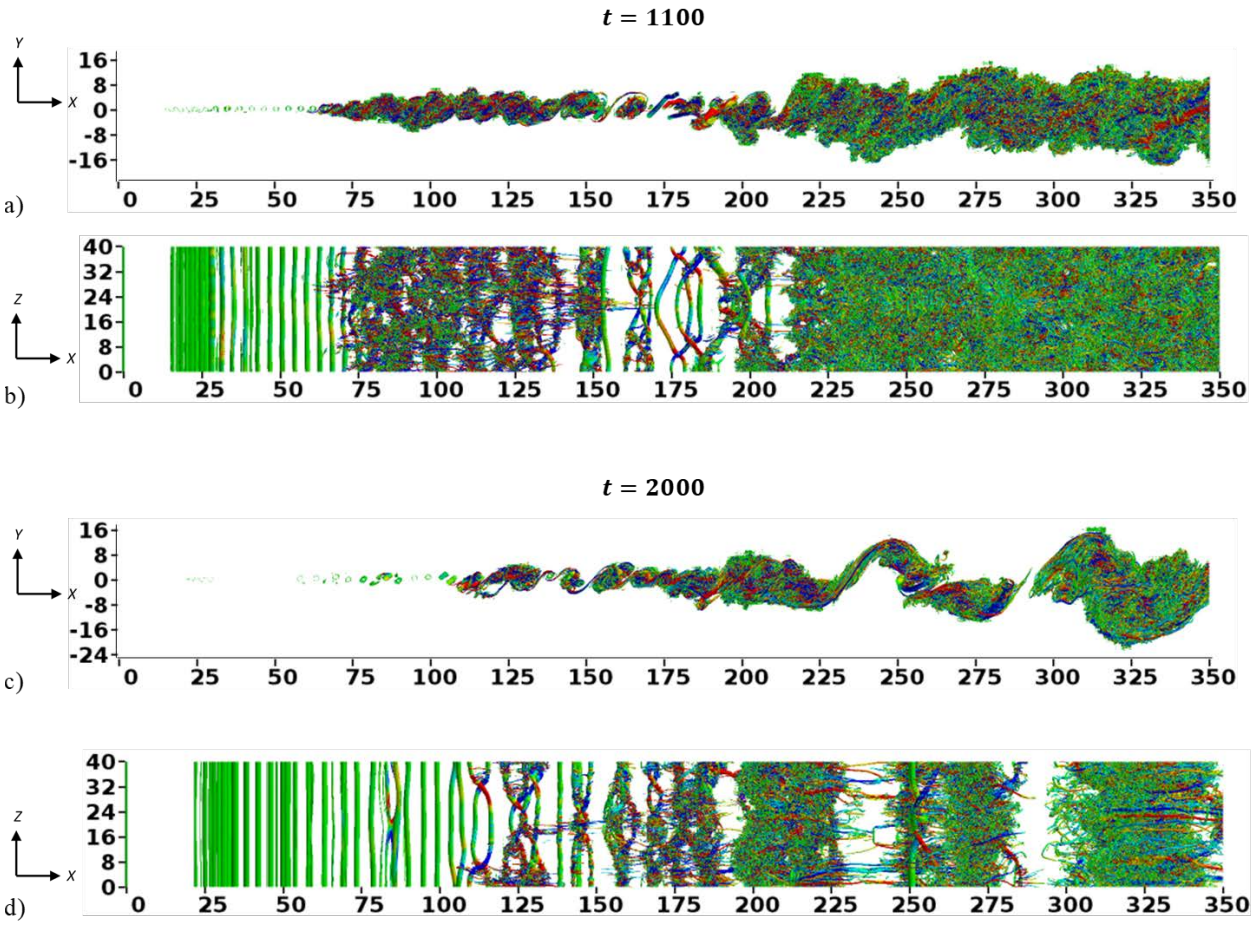

Fig. A3 Plan views of vortex structures obtained in the Case V simulations at at $t = 1100$ (a,b) and $t = 2000$ (c,d) using iso-surfaces at $\lambda_2 = -0.001$. Notations are the same as in Fig. A1. All axes are normalized with δ_1.